Benchmarking a two-way coupled coastal wave-current hydrodynamics model

Anastasia K. Fragkou[1*], Christopher Old[2], Vengatesan Venugopal[3], Athanasios Angeloudis[4]

[1] PhD Student
School of Engineering, Institute for Infrastructure and the Environment, University of Edinburgh, Edinburgh, UK
Email address: a.fragkou@ed.ac.uk

[2] Research Associate
School of Engineering, Institute for Energy Systems, University of Edinburgh, Edinburgh, UK
Email address: c.old@ed.ac.uk

[3] Professor
School of Engineering, Institute for Energy Systems, University of Edinburgh, Edinburgh, UK
Email address: v.venugopal@ed.ac.uk

[4] Lecturer
School of Engineering, Institute for Infrastructure and the Environment, University of Edinburgh, Edinburgh, UK
Email address: a.angeloudis@ed.ac.uk

Benchmarking a two-way coupled coastal wave-current hydrodynamics model

Anastasia K. Fragkou[a,*], Christopher Old[b], Vengatesan Venugopal[b], Athanasios Angeloudis[a]

[a] *School of Engineering, Institute for Infrastructure and the Environment, University of Edinburgh, Edinburgh, UK*

[b] *School of Engineering, Institute for Energy Systems, University of Edinburgh, Edinburgh, UK*

Abstract

Wave-current interaction phenomena are often represented through coupled model frameworks in ocean modelling. However, the benchmarking of these models is scarce, revealing a substantial research challenge. We seek to address this through a selection of benchmark cases for coupled wave-current interaction modelling frameworks. This comprises a series of analytical and experimental test cases spanning three diverse conditions of wave run-up, one scenario of waves opposing a current flow, and a 2-D arrangement of waves propagating over a submerged bar. We simulate these through coupling of the spectral wave model, Simulating WAves Nearshore (SWAN), with the coastal hydrodynamics shallow-water equation model, Thetis, through the Basic Model Interface (BMI) structure. In our analysis, by comparing calibrated versus default parameter settings we identify and highlight calibration uncertainties that emerge across a range of potential applications. Calibrated model results exhibit good correlation against experimental and analytical data, alongside benchmarked wave-current model predictions, where available. Specifically, inter-model comparisons showcase equivalent accuracy. Finally, the coupled model we developed as part of this work showcases its ability to account for wave-current effects, in a manner extensible to other coupled processes through BMI and applicable to more complex geometries.

Keywords: Wave-current interactions, Coupled model, Shallow-water equation modelling, Spectral wave modelling, Validation

1. Introduction

Wave-current interaction phenomena are common in coastal areas, where both surface gravity waves and ocean currents become influential to coastal hydrodynamics simultaneously Wolf and Prandle (1999). In such cases, their concurring presence affects each other; wave transformation processes generate radiation stress and are influenced by the water depth and the presence of underlying currents. Radiation stress in turn affects currents and wave setup, compounded by bottom friction and vertical mixing (Dietrich et al., 2011). Accurate representation of such interactions is motivated by a plethora of applications, such as capturing evolution of coastal morphology (Santos et al., 2009), design of offshore and coastal infrastructure (Brown, 2010), or quantifying storm surge effects (Zhang et al., 2021).

The need to account for wave-current interactions was recognised early (Longuet-Higgins and Stewart, 1962; Jonsson et al., 1970; Peregrine, 1976), leading to the development of coupled ocean and spectral wave models. The first coupled model configurations, as well as some later ones, employ a structured mesh, either orthogonal (Xie et al., 2001; Xia et al., 2004; Marsooli et al., 2017) or curvilinear (Warner et al., 2008; Kumar et al., 2011); such a configuration could

*Corresponding author
Email address: `a.fragkou@ed.ac.uk` (Anastasia K. Fragkou)

potentially incur high computational costs when multiple scales must be resolved. In increasing versatility through multi-scale modelling, unstructured coupled models followed (Dietrich et al., 2011; Roland et al., 2012; Zhang et al., 2016; Dobbelaere et al., 2022). Alternative solutions were also presented that maintained independent discretisation allowing greater flexibility among model-components (Dutour Sikirić et al., 2013). Wave-current interaction models are notoriously difficult to validate. It is challenging to establish validation data for wave-current interactions at regional scales, as a fully controlled environment at such scales becomes unattainable. Hence, models are often applied to either idealised cases focusing on an indirect validation by examining other processes of interest like sediment transport (Warner et al., 2008) or more realistic setups on the effect of wave-current interactions that contain a large margin of uncertainties (Dietrich et al., 2011; Xie et al., 2001), especially during extreme events, such as hurricane conditions (Dobbelaere et al., 2022). A few studies demonstrated efforts to validate the modelling through analytical or experimental test cases where wave-current interactions emerge (Roland et al., 2012; Marsooli et al., 2017; Kumar et al., 2011). It is instructive to provide an overview of the models themselves, presenting features that motivate this research. In the process, we include details to highlight the diversity of coupled modelling frameworks.

We begin with the study of Roland et al. (2012) on the coupling between the unstructured 3-D hydrodynamic model SELFE (Zhang and Baptista, 2008) and the phase-averaged spectral wave model Wind Wave Modell II (WWM-II; Roland 2008). The former applies a semi-implicit time-marching scheme, while the advection is propagated through an Eulerian-Lagrangian method, which ensures model numerical stability. The coupling of the two models is inherently integrated by including WWM-II in SELFE's source code as a routine, with both models written in Fortran. The coupled framework's ability to account for wave-current interactions is evaluated through a series of analytical and experimental setups, validating its capacity for a plethora of phenomena were wave-current interactions are dominant. SELFE has expanded into the Semi-Implicit Cross-scale Hydroscience Integrated System Model (SCHISM; Zhang et al. 2016) preserving its coupling with WWM-II.

In turn, we have the study of Marsooli et al. (2017) who validated their model through the numerical implementation of a series of experimental setups. The coupled framework consists of the 3-D Stevens Institute of Techonology Estuarine and Coastal Ocean Model (sECOM; Blumberg and Mellor 1987) and the Mellor-Donelan-Oey (MDO; Mellor et al. 2008) spectral wave model where the same Arakawa C orthogonal curvilinear grid with terrain-following vertical coordinates employed for both components. The wave model, simpler than 3rd generation wave models in omitting the solution of the spectral equation in the frequency space (Mellor et al., 2008), solves the wave energy balance equation accounting for current-induced refraction alongside the deep- and shallow-water phenomena. It employs the spectrum of Donelan et al. (1985), which makes the wave-wave interaction in the frequency space parametrisation computationally effective. However to the best of our knowledge, MDO relied on serial computation, which in combination with its structured setup could hinder the scalability of any coupled model.

Lastly, we refer to the coupled model of Xie et al. (2001) consisting of the structured 3-D ocean circulation model Princeton Ocean Model (POM; Mellor 1998) and the spectral WAve Model (WAM; Komen et al. 1996). In Xie et al. (2001), the coupled model was immediately applied for the simulation of a practical case, the South Atlantic Bight (Xie et al., 2001). Subsequently, when Xia et al. (2004) incorporated into the coupled model an extended formulation of radiation stress in the vertical direction, some benchmarking using the analytical solution of Longuet-Higgins and Stewart (1964) was reported towards demonstrating the validity of their formulation.

Considering the broad associated literature that apply wave-current interaction models, we observe that only a minority of wave-current coupled models report on validation of wave-current phenomena at controlled environments, as regulating the various parameters at regional scales becomes a challenging task. Therefore, this work documents our efforts towards a validated coupled model to capture wave-current interactions. Our objective is to do so in an efficient manner while being mindful of (a) parallelisation and scalability requirements, (b) the continuous development of the individual models, and (c) coupled-model extensions to other processes (e.g. atmospheric). The latter would render a non-intrusive coupling configuration important for future development.

In this study, the spectral wave model Simulating WAves Nearshore (SWAN; Booij et al. 1999) is coupled with the shallow-water equation model, Thetis (Kärnä et al., 2018; Kärnä, 2020). This coupled framework (presented in Section 2) is the first 2-D model for wave-current interactions that uses a collection of validation cases (Section 3) comprised of analytical and experimental setups, while comparing its performance with other coupled models (Section 4). Furthermore, an effort is made to outline the calibration rationale for the cases considered and the applications of the coupled framework (Section 5). Finally, in maintaining versatility of the coupling framework we refactor model elements to use a minimally-intrusive interface in Python, preserving the processing efficiency of Fortran and C++ code for the iterative solving of SWAN and Thetis, respectively.

2. Methodology

2.1. Spectral Wave Model

The spectral wave model SWAN solves the action density equation to calculate wave characteristics and spectra

$$\underbrace{\frac{\partial N}{\partial t}}_{1} + \underbrace{\nabla_{x,y} \cdot (\boldsymbol{c}_{x,y} N)}_{2} + \underbrace{\nabla_{\sigma,\theta} \cdot (\boldsymbol{c}_{\sigma,\theta} N)}_{3} = \frac{1}{\sigma} \sum S \tag{1}$$

where

$$\sum S = S_{\text{in}} + S_{\text{ds}} + S_{\text{nl}} + S_{\text{bf}} + S_{\text{brk}} \tag{2}$$

The action density N expresses the ratio of the energy density E over the relative frequency σ. On the LHS, term 1 of Eq. [1] denotes the changes of action density N in time t, while term 2 expresses its advection in the geographical domain with propagation speed $\boldsymbol{c}_{x,y}$. Term 3 represents the shifting of frequencies in the frequency (σ) domain and the refraction in the wave direction (θ) domain with propagation speed $\boldsymbol{c}_{\sigma,\theta}$. The RHS of Eq. [1] comprises the sum of the source and sink terms (Eq. [2]), which include the wind input (S_{in}), whitecapping dissipation (S_{ds}), non-linear wave-wave interactions (S_{nl}), bottom friction (S_{bf}) and depth-induced wave-breaking (S_{brk}) effects (see Booij et al. (1999) for details).

Bed friction is considered through the eddy-viscosity model of Madsen et al. (1989) where energy dissipation due to bottom friction is expressed as

$$S_{\text{bf}} = -C_b \frac{\sigma^2}{g^2 \sinh^2(kh)} E(\sigma, \theta) \tag{3}$$

where C_b is a bottom friction coefficient, σ is the relative radian frequency, k is the wavenumber, h is the water depth, and E is the energy density spectrum. Madsen et al. (1989) takes into account the bottom roughness height and the actual wave conditions for the calculation of the bottom friction coefficient (SWAN Team, 2019).

For the calculation of the energy dissipation due to depth-induced wave-breaking, SWAN extends the expression of Eldeberky and Battjes (1996) to include the spectral directions

$$S_{\mathrm{brk}}(\sigma,\theta) = \frac{\alpha_{BJ}\, Q_b \tilde{\sigma}}{\beta^2 \pi} E(\sigma,\theta) \tag{4}$$

where S_{brk} is the energy dissipation due to depth-induced wave-breaking, α_{BJ} is the rate of energy dissipation, Q_b is the fraction of breaking waves, $\tilde{\sigma}$ is the mean frequency, β is the ratio of root mean square wave height (H_{rms}) over maximum water height ($H_{\max}$). In turn, the latter adheres to $H_{\max} = \gamma h$, where γ is the breaker index expressing the ratio of wave height and still water depth at the location waves start breaking (Holthuijsen, 2010).

In non-stationary SWAN simulations, a first-order semi-Lagrangian scheme, called Backward Space Backward Time (BSBT), is employed for propagating in time and space (SWAN Team, 2019). Here, the structured rectilinear formulation of SWAN is employed either serially or in parallel.

2.2. Shallow-water Equation Model

Thetis, a 2-D/3-D coastal model (Kärnä et al., 2018), employs the Firedrake finite element modelling framework, which uses abstraction for the description of the weak formulation of PDEs and the generation of automated code (Rathgeber et al., 2016). It considers the non-conservative formulation of the shallow water equations (Eq. [5], [6]). The model accounts for wetting and drying by utilizing the formulation of Kärnä et al. (2011) introducing a modified bathymetry to ensure positive water depth as defined by Eq. [7]. Therefore,

$$\frac{\partial \eta}{\partial t} + \frac{\partial \tilde{h}}{\partial t} + \nabla \cdot \left(\tilde{H}_d \boldsymbol{u}\right) = 0 \tag{5}$$

$$\frac{\partial \boldsymbol{u}}{\partial t} + \boldsymbol{u} \cdot \nabla \boldsymbol{u} + g \nabla \eta = \nabla \cdot \left(\nu \left(\nabla \boldsymbol{u} + \nabla \boldsymbol{u}^T\right)\right) - \frac{\boldsymbol{\tau_b} + \boldsymbol{\tau_{rs}} + \boldsymbol{\tau_{wr}}}{\rho \tilde{H}_d} \tag{6}$$

$$f(H_d) = \frac{1}{2}\left(\sqrt{H_d^2 + \alpha_{wd}^2} - H_d\right) \tag{7}$$

where η is the water elevation, $H_d = h + \eta$ is the total water depth, $\boldsymbol{u}$ is the depth-averaged velocity vector, ν is the kinematic viscosity of the fluid, and α_{wd} is a wetting and drying parameter. The latter through Eq. [7] modifies the bathymetry $\tilde{h} = h + f(H_d)$, with an equivalent treatment for the modified total water depth $\tilde{H}_d$. The bed shear stress effects ($\boldsymbol{\tau_b}$) make use of the Manning formulation with a friction coefficient n_M, so that

$$\frac{\boldsymbol{\tau_b}}{\rho} = g n_M^2 \frac{|\boldsymbol{u}|\, \boldsymbol{u}}{H_d^{1/3}} \tag{8}$$

while the effect of the radiation stress caused by waves is described by the term $\boldsymbol{\tau_{rs}}$ and the effect of the wave roller by $\boldsymbol{\tau_{wr}}$ [see Section 2.4 for more information].

The shallow-water equations in this study are discretised using the discontinuous Galerkin finite element method (DG-FEM). The semi implicit Crank-Nicolson scheme, imposing an implicitness $\theta = 0.5$, time marches the solution in all cases. The resulting system of equations is sequentially solved iteratively by Newton's method as implemented in PETSc (Balay et al., 2019).

2.3. *Basic Model Interface*

The coupled model is facilitated by the Basic Model Interface (BMI; Hutton et al. 2020), a library of functions provided across several programming languages. The functions are categorised as: (i) *model control functions* to call a component of the model to bypass the mainstream time-loop, (ii) *model information functions* that provide general information about the exchange variables, (iii) *variable information functions* to supply details about a particular input or output field, (iv) *time functions* to administer information on the model times, (v) *variable getter and setter functions* to access and modify the exchange items of the models, and (vi) *model grid functions* to describe the model spatial discretisation[1].

The two models have been refactored to fit into a BMI "template", which is constructed in Fortran for SWAN and in Python for Thetis. Due to the differing programming languages utilised by each model, SWAN was converted into a Python package for invocation by Python through utilising the refactored SWAN source code, which is then fitted into the Fortran 2003 BMI template. By wrapping the latter with a C interoperability layer, SWAN can be compiled and linked in a C library. This library can be called from Cython, an extension language that enables a C library to be called from Python. As such, the 'cythonised' code can be converted into a Python package (Fig. 1).

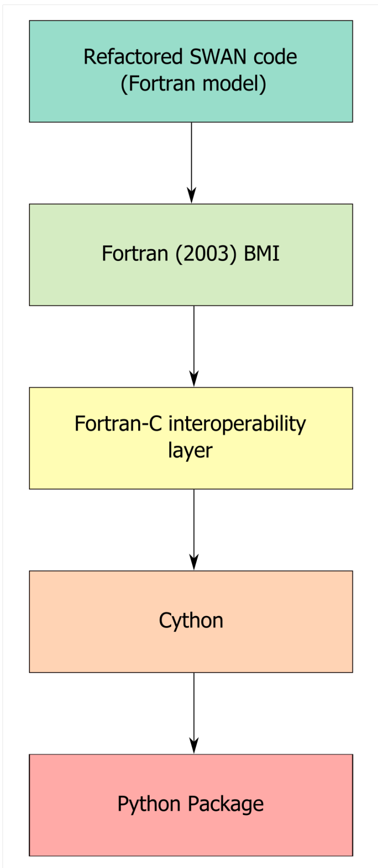

Figure 1: SWAN: The conversion from Fortran code to a Python package

[1] see https://bmi.readthedocs.io/en/latest/ for more details

2.4. Coupling Procedure

The parallel coupling procedure commences by initialising SWAN followed by Thetis, allowing for internal *"on the fly"* communication. The two models run on an iterative basis, marching forward following their own time-stepping mechanism, with Δt_{SWAN} for SWAN, and $\Delta t_{\mathrm{Thetis}}$ for Thetis. The time t in Fig. 2 is the time that the two models are required to reach to exchange the necessary information through BMI and is used to coordinate the serial implementation of the model components. As such, the coupling time-step $\Delta t_{coupling}$, i.e. the time interval between information exchange, is a multiple of both time-steps. Initialisation of Thetis and SWAN launches the coupling procedure which iterates the process until the simulation end time, t_{end}.

SWAN provides the necessary statistical wave parameters for the calculation of the radiation stress and the wave roller contribution. These parameters are the significant wave height, H_s, the wave direction, θ_m, the wavelength, λ, and the percentage of wave-breaking, Q_b. In turn, Thetis provides SWAN with water elevation, η, and current, $\boldsymbol{u}$, information.

We adopt the calculation of vertically integrated radiation stress proposed by Mellor (2015)

$$\overline{S_{ij}}^{z} = E\left[n\frac{k_i k_j}{k^2} + \delta_{ij}\left(n - \frac{1}{2}\right)\right] \tag{9}$$

where $\overline{S_{ij}}^{z}$ is the vertically integrated radiation stress, n is the ratio of the group over the phase velocity, k is the wavenumber, and δ_{ij} is the Kronecker delta function (1 when $i = j$ or 0 otherwise). The gradient of $\overline{S_{ij}}^{z}$ describes the radiation stress on currents

$$\boldsymbol{\tau_{rs}} = \nabla\overline{S_{ij}}^{z} \tag{10}$$

The vertically integrated effect of the roller-wave interface is calculated similarly (Reniers and Battjes, 1997; Svendsen, 1984) as

$$R_{ij} = 2E_r\frac{k_i k_j}{k^2} \tag{11}$$

where $E_r = \rho g A_r \sin\phi$ is the energy due to roller wave interface according to Duncan (1981), where $A_r = 0.9H^2$ (Svendsen, 1984) the roller area and ϕ the roller angle with $\tan\phi \approx 0.1$ (Reniers and Battjes, 1997) generally accepted (Martins et al., 2018). The gradient of R_{ij} yields the effect of wave-rollers on currents

$$\boldsymbol{\tau_{wr}} = \nabla R_{ij} \tag{12}$$

The combined effect of waves on currents is the sum of the gradient of radiation stress and the wave-roller effects, $\boldsymbol{\tau_{rs}} + \boldsymbol{\tau_{wr}}$.

3. Case studies

A series of analytical and experimental setups of varying complexity (Table 1) are employed to validate the model's capability to accurately capture wave-current interactions, and evaluate performance against other models. First we consider the idealised setup for the analytical solution developed by Longuet-Higgins and Stewart (1964), where wave-setup is validated against an analytical solution. Next, we move to the case of Boers (1997) that considers a more realistic bathymetry that leads to wave setup, depth-induced wave-breaking, and bed friction losses. In turn, the case of Roelvink and Reniers (1995) explores the same effects at a scale that is closer to regional coastal applications. We then examine the model's ability in the presence of a strong opposing current adopting the Lai et al. (1989) experiment. Finally, we consider the 2-D experimental setup (Dingemans, 1987) of a submerged bar subjected to wave action.

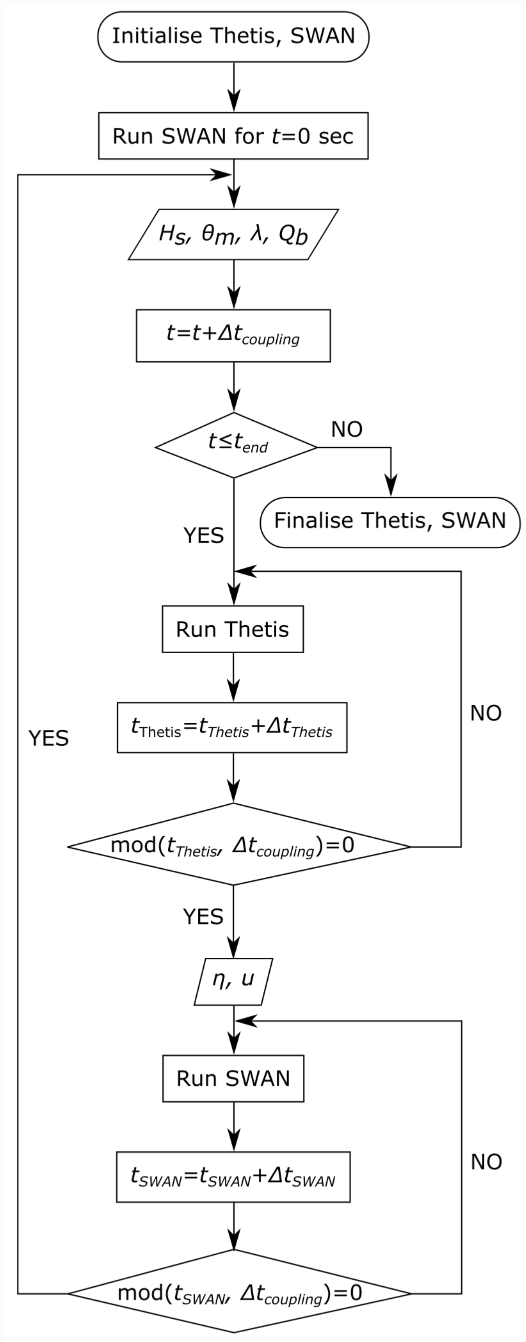

Figure 2: Flowchart of the integrated coupling between the structured SWAN and Thetis

In all cases the mesh generation for Thetis employs the open-source *qmesh* (Avdis et al., 2018) package, returning an unstructured triangular mesh. The mesh employed by SWAN is a structured orthogonal mesh constructed internally by SWAN. For each case a nested setup is utilised composed of two domains: domain D_1, i.e. the outer domain in which only SWAN is implemented; and D_2: the area of interest where the coupled model is applied (Fig. 3). D_1 provides the top (N) and bottom (S) wave boundary conditions for the latter domain in these setups. To conserve computational resources, stationary conditions are applied in domain D_1, while a stationary SWAN run of D_2 is executed to spin-up the wave conditions before a coupled model is implemented.

Table 1: Test cases employed for the coupled model's validation

Case	Type	Depth range [m]	Phenomena
Longuet-Higgins and Stewart (1964)	Analytical	$[0.05, 0.45]$	Depth-induced wave-breaking, Wave setup
Boers (1997)	Experimental	$[0.05, 0.80]$	Depth-induced wave-breaking, Wave setup, Bottom friction
Roelvink and Reniers (1995)	Experimental	$[0.20, 4.10]$	Depth-induced wave-breaking, Wave setup, Bottom friction, Undertow current, Deeper bathymetry
Lai et al. (1989)	Experimental	$[0.45, 0.75]$	Strong opposing current, Wave blocking
Dingemans (1987)	Experimental	$[0.10, 0.40]$	Submerged bar in 2-D configuration

Sensitivity analyses are performed to examine the effect of model (SWAN/Thetis) parameters on the results to balance accuracy and computational cost. For SWAN, these include the geographical mesh spacing (where $dx = dy$), timestep Δt_{SWAN}, limits of spectral wave direction $[\theta_1, \theta_2]$ alongside the spectral resolution $\Delta\theta$, standard directional deviation of wave spreading σ_θ, the equivalent roughness length k_n implemented in the bed friction losses formulation of SWAN, the rate of dissipation for depth-induced wave-breaking α_{BJ} followed by the maximum wave height over water depth ratio γ. In addition, the effects of triad wave-wave interactions and whitecapping dissipation were tested. In Thetis, the sensitivity explores effects of mesh element length $\wedge h$, timestep Δt_{Thetis}, kinematic viscosity ν, wetting and drying α_{wd} and the manning coefficient n_M. The most salient observations of the sensitivity analyses are discussed in Section 5.1 while the calibrated configurations, resulting in improved predictions, are described here for each of the cases. The "default" setup including initial parameters is summarised in Table 3 for each case. For SWAN, these follow recommended values of Booij et al. (2004), apart from the standard directional deviation of wave spreading, as wave conditions listed in Table 2 are narrow-banded. Similarly, Thetis default parameters employ typical values for regional coastal-scale simulations (such as $n_M = 0.03$). The model mesh size was defined through a mesh convergence process that initiated from coarse configurations to reduce computational cost.

3.1. Longuet-Higgins and Stewart (1964) case on wave set-up on a linearly sloped beach

Longuet-Higgins and Stewart (1964) provided an analytical solution for wave set-up in a gradually varying beach for 1-D steady state situations. The momentum balance is

$$\frac{d\eta}{dx} = -\frac{1}{\rho g h}\frac{dS_{xx}}{dx}. \tag{13}$$

In the absence of reflection outside the surf zone, we can assume wave energy continuity

$$\frac{dEc_g}{dx} = 0 \tag{14}$$

where S_{xx} is the radiation stress and c_g the group velocity. In the surf zone, the wave height is controlled by $H = \gamma h$. Solving Eq. [13] considering the aforementioned assumptions results in two areas: (i) the outer zone; and (ii) the surf zone. The boundary between the two is denoted by coordinate x_B. In the outer zone, i.e. for $x \geq x_B$, the water elevation is described by

$$\eta = -\frac{a^2 k}{2\sinh(2kh)} \tag{15}$$

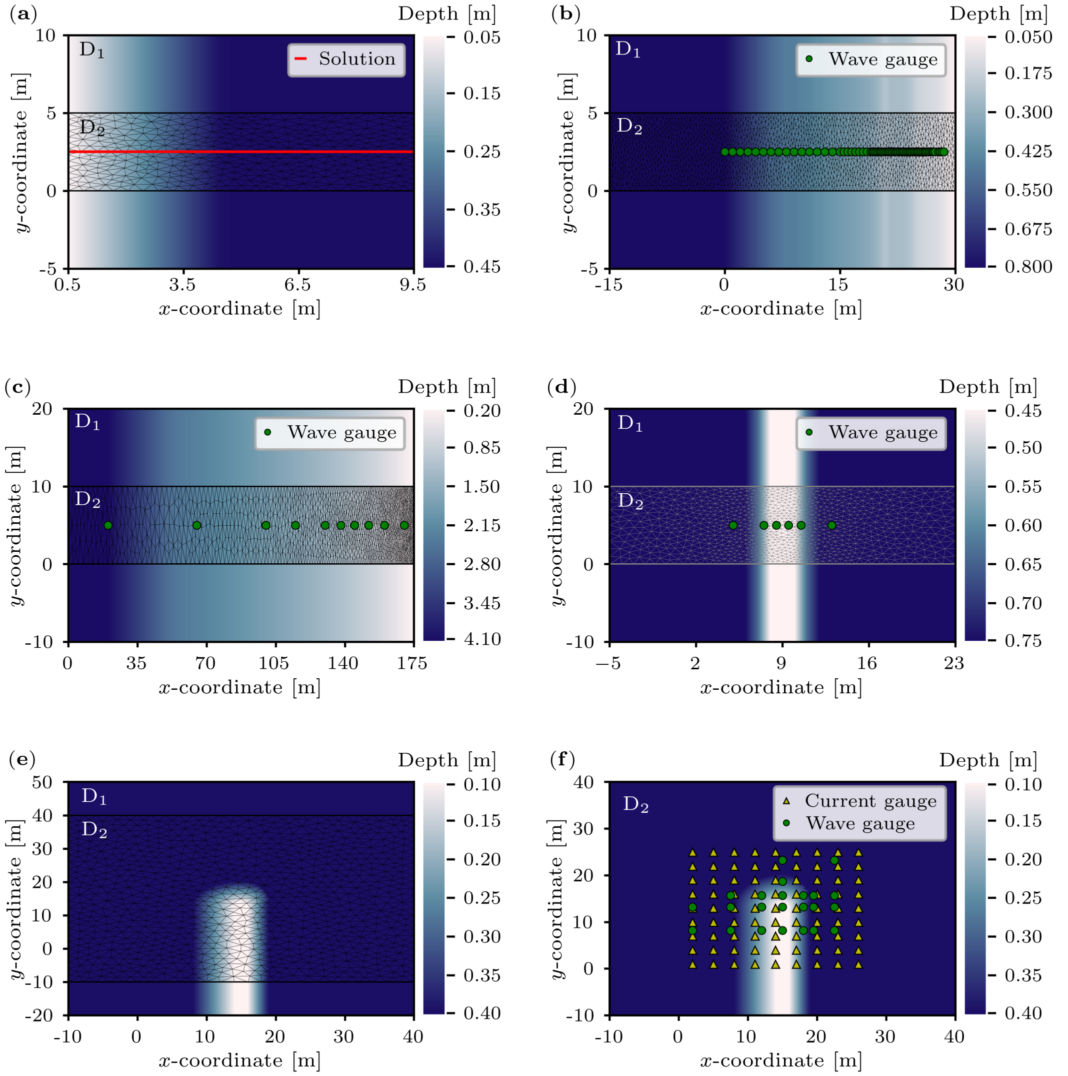

Figure 3: Computational domain for: (a) the Longuet-Higgins and Stewart (1964) case; (b) the Boers (1997) experiment; (c) the Roelvink and Reniers (1995) setup; (d) the Lai et al. (1989) study; (e) the Dingemans (1987) experiment; and (f) close-up to the nested domain of the Dingemans (1987) domain. All domains are comprised of the outer domain D_1 and the nested domain D_2 where the coupled model is implemented. The unstructured mesh depicted in figures (a)-(e) is employed by Thetis.

while from the wave energy conservation, we have

$$\frac{a^2}{k}\left(\frac{2kh}{\sinh 2kh}+1\right)=\frac{a_0^2}{k_0} \tag{16}$$

where a is the local wave amplitude, k is the wavenumber, and the subscript "0" indicates deep water parameters. Within the surf zone, i.e. for $x < x_B$, as wave amplitude is proportional to local water depth, the water elevation is

$$\eta=\frac{1}{1+\frac{8}{3\gamma^2}}\left(h_B-h\right)+\eta_B \tag{17}$$

with the subscript "B" denoting quantities at the boundary between the outer and surf zones. As the water elevation at the boundary has to be continuous, equating Eq. [15] with Eq. [17]

Table 2: Boundary conditions for the cases depicted in Fig. 3, where N represents the top boundary, E is the right boundary, S the bottom boundary and W is the left boundary.

Case \ Boundary		SWAN N	SWAN E	SWAN S	SWAN W	Thetis N	Thetis E	Thetis S	Thetis W
Longuet-Higgins and Stewart (1964)		From D_1	$H = 0.18$ m, $T_p = 1.50$ s	From D_1	Shore	$Q = 0$ m^3 s^{-1}	$\eta = -0.0024$ m	$Q = 0$ m^3 s^{-1}	$u_n = 0$ m s^{-1} †
Boers (1997)	Exp. A	From D_1	Shore	From D_1	$H_s = 0.16$ m, $T_p = 2.10$ s	$Q = 0$ m^3 s^{-1}	$u_n = 0$ m s^{-1}	$Q = 0$ m^3 s^{-1}	$\eta = -0.0008$ m
	Exp. B	From D_1	Shore	From D_1	$H_s = 0.21$ m, $T_p = 2.10$ s	$Q = 0$ m^3 s^{-1}	$u_n = 0$ m s^{-1}	$Q = 0$ m^3 s^{-1}	$\eta = -0.0198$ m
	Exp. C	From D_1	Shore	From D_1	$H_s = 0.10$ m, $T_p = 3.40$ s	$Q = 0$ m^3 s^{-1}	$u_n = 0$ m s^{-1}	$Q = 0$ m^3 s^{-1}	$\eta = -0.0002$ m
Roelvink and Reniers (1995)		From D_1	Shore	From D_1	$H_s = 0.95$ m, $T_p = 5.00$ s	$Q = 0$ m^3 s^{-1}	$Q = 0$ m^3 s^{-1}	$Q = 0$ m^3 s^{-1}	$\eta = -0.023$ m
Lai et al. (1989)		From D_1	Unspecified*	From D_1	$H = 0.01$ m, $T_p = 0.57$ s	$Q = 0$ m^3 s^{-1}	$u = -0.13$ m s^{-1}, $v = 0.00$ m s^{-1} ×	$Q = 0$ m^3 s^{-1}	$u = -0.13$ m s^{-1}, $v = 0.00$ m s^{-1}
Dingemans (1987)		From D_1	Unspecified*	From D_1	$H_s = 0.10$ m, $T_p = 1.25$ s	$Q = 0$ m^3 s^{-1}	$u_n = 0$ m s^{-1}	$Q = 0$ m^3 s^{-1}	$Q = 0$ m^3 s^{-1}

* When the wave BC is unspecified, SWAN assumes that no waves enter the domain from this boundary and waves can leave the domain freely (Booij et al., 2004)

† u_n is the normal velocity to the boundary

× The current velocities u, v are given in problem coordinates

and including the dispersion relationship, (Eq. [18])

$$\omega = \sqrt{gk \tanh kh}, \tag{18}$$

and the energy conservation (Eq. [14]), we determine the location of x_B. The system of equations has been solved for $dx = 0.125$ m (Fig. 3a, red line).

In comparing our model to the analytical solution, we apply a monochromatic wave of amplitude $a = 0.09$ m and period $T = 1.5$ s with normal incident direction to the shore on the nested setup of Fig. 3a, following the modelling study of Roland et al. (2012) and Xia et al. (2004). The bathymetry is constant in the y-direction, while in the x-direction it is flat with still water depth $h = 0.45$ m for $x \geq 4.5$ m. For $x < 4.5$ m, the depth decreases linearly to $h = 0.05$ m by a slope of 0.1. The numerical domain starts at $x = 0.5$ m (dotted line in Fig. 4) due to SWAN's limitation in predicting wave characteristics in very shallow water depths. SWAN mesh spacing is $dx = dy = 0.4$ m, whereas Thetis employs an unstructured mesh with an element length $\wedge h = 0.4$ m (Table 3).

In terms of boundary conditions (Table 2), the wave condition is applied at the right boundary of SWAN. For Thetis, the calculated water elevation from the analytical solution is also imposed there. The left Thetis boundary represents the shore and a no-slip condition is set, whilst a free-slip boundary condition is utilised on the remaining boundaries. The only physical process taken into account in SWAN is the depth-induced wave-breaking with maximum wave height over water depth ratio $\gamma = 0.83$ (following Roland et al. (2012) and Xia et al. (2004)) and rate of dissipation $\alpha_{BJ} = 1.5$, while we neglect any energy losses due to bottom friction and wind-driven waves. Thetis also disregards bed friction losses. Following sensitivity, SWAN's timestep is $\Delta t_{\text{SWAN}} = 20$ s, whereas $\Delta t_{\text{Thetis}} = 1$ s with a coupling timestep ($\Delta t_{\text{coupling}}$ equal to the largest of the two (Table 3).

3.2. Boers (1997) case on surf zone with a barred beach

Boers (1997) examined depth-induced wave-breaking and wave-induced set-up under laboratory conditions. By use of a flume with length 40 m, width 0.8 m and height 1.08 m, they recorded the evolution of random unidirectional waves over a bar trough profile. The

Table 3: Synoptic presentation of the "default" (D.) and the calibrated (C.) values derived by the sensitivity analyses.

Case		Longuet-Higgins and Stewart (1964)		Boers (1997) Exp. A		Boers (1997) Exp. B		Boers (1997) Exp. C		Roelvink and Reniers (1995)		Lai et al. (1989)		Dingemans (1987)	
Variable	Notation [units]	D.	C.	D.	C.	D.	C.	D.	C.	D.	C.	D.	C.	D.	C.
SWAN															
Geographical mesh spacing	$dx = dy$ [m]	0.4	0.4	-*	0.4*	0.4	0.4	-*	0.4*	5.0	5.0	0.4	0.5	0.4	2.0
Timestep	Δt_{SWAN} [s]	1	20	-*	10*	1	10	-*	10*	1	3	1	20	1	60
Minimum wave direction	θ_1 [^{o}]	175	175	-*	-10*	-10	-10	-*	-10*	-10	-10	-10	-10	-70	-50
Maximum wave direction	θ_2 [^{o}]	185	185	-*	10*	10	10	-*	10*	10	10	10	10	10	10
Spectral directional resolution	$\Delta\theta$ [^{o}]	1.0	2.5	-*	2.0*	1.0	2.0	-*	2.0*	1.0	1.0	0.5	4.0	11.4	12.0
Directional standard deviation	σ_θ [^{o}]	1.5	2.0	1.0	1.1	1.0	1.0	1.0	0.7	1.0	1.0	2.5	5.0	2.5	2.5
Equivalent roughness length scale	k_n [m]	-	-	-*	0.02*	0.05	0.02	-*	0.02*	0.05	0.05	0.05	-	0.05	0.04
Rate of depth-induced wave-breaking dissipation	α_{BJ} [-]	1.0	1.5	-*	1.5*	1.0	1.5	-*	1.5*	1.0	1.0	1.0	-	1.0	1.0
Breaker index	γ [-]	0.83	0.83	-*	0.63*	0.73	0.63	-*	0.63*	0.73	0.73	0.73	-	0.73	0.73
Thetis															
Mesh spacing	$\wedge h$ [m]	0.4	0.4	-*	0.4*	0.4	0.4	-*	0.4*	1.0	$[0.5, 2.5]$	0.4	$[0.4, 1.0]$	0.4	2.0
Timestep	Δt_{Thetis} [s]	1	1	-*	5*	1	5	-*	5*	1	3	1	2	1	1
Kinematic viscosity	ν [m^2/s]	1.00	1.00	-*	0.25*	0.50	0.25	-*	0.25*	0.50	1.00	$[0.50, 5.00]$	$[0.25, 3.80]$	0.50	0.01
Wetting and drying parameter	α_{wd} [m]	0.5	0.1	-*	0.5*	0.5	0.5	-*	0.5*	0.5	2.5	-	-	0.5	-
Manning coefficient	n_M [-]	-	-	-*	-*	0.030	-	-*	-*	0.030	-	0.030	-	0.030	0.022

* Indicates that sensitivity analysis took place only for case B. The calibrated value was used for the cases A and C

Table 4: Synoptic demonstration of the ranges examined during the sensitivity analyses

Variable	Notation [units]	Longuet-Higgins and Stewart (1964)	Boers (1997) Exp. A	Boers (1997) Exp. B	Boers (1997) Exp. C	Roelvink and Reniers (1995)	Lai et al. (1989)	Dingemans (1987)
SWAN								
Geographical mesh spacing	$dx = dy$ [m]	[0.1, 0.5]	N/A*	[0.1, 0.5]	N/A*	[0.5, 5.0]	[0.2, 1.0]	[0.2, 2.5]
Timestep	Δt_{SWAN} [s]	[1, 30]	N/A*	[1, 30]	N/A*	[1, 5]	[1, 60]	[1, 60]
Minimum wave direction	θ_1 [^{o}]	[95, 180]	N/A*	[-90, -10]	N/A*	[-90, -10]	[-90, -10]	[-90, -10]
Maximum wave direction	θ_2 [^{o}]	[180, 265]	N/A*	[10, 90]	N/A*	[10, 90]	[10, 90]	[10, 90]
Spectral directional resolution	$\Delta\theta$ [^{o}]	[0.25, 5.00]	N/A*	[0.5, 2.5]	N/A*	[0.5, 5.0]	[0.5, 4.0]	[1.0, 30.0]
Directional standard deviation	σ_θ [^{o}]	[0.25, 2.50]	[0.5, 2.0]	[0.5, 2.5]	[0.5, 2.0]	[0.5, 7.5]	[0.5, 15.0]	[0.5, 10.0]
Equivalent roughness length scale	k_n [m]	N/A†	N/A*	[0.00, 0.06]	N/A*	[0.00, 0.15]	[0.00, 0.09]	[0.00, 0.07]
Rate of depth-induced wave-breaking dissipation	α_{BJ} [-]	[0.5, 2.5]	N/A*	[0.5, 2.5]	N/A*	[0, 2]	[0.0, 2.5]	[0.0, 2.5]
Breaker index	γ [-]	[0.68, 0.88]	N/A*	[0.53, 0.93]	N/A*	[0.53, 0.93]	N/A†	[0.43, 0.93]
Thetis								
Mesh spacing	$\wedge h$ [m]	[0.1, 0.5]	N/A*	[0.1, 0.4]	N/A*	[0.5, 4.0]	[0.2, 1.0]	[0.2, 2.5]
Timestep	$\Delta t_{\mathrm{Thetis}}$ [s]	[1, 10]	N/A*	[1, 20]	N/A*	[1, 12]	[1, 5]	[1, 15]
Kinematic viscosity	ν [m^2/s]	[0.1, 1.0]	N/A*	[0.1, 1.0]	N/A*	[0.1, 1.5]	[0.1, 1.0] / [1, 5] ×	[0.01, 1.00]
Wetting and drying parameter	α_{wd} [m]	[0.0, 0.5]	N/A*	[0.0, 1.0]	N/A*	[0, 3]	[0.0, 0.2]	[0, 1]
Manning coefficient	n_M	N/A*	N/A*	[0.00, 0.04]	N/A*	[0.00, 0.04]	[0.00, 0.06]	[0.00, 0.04]

* Indicates that sensitivity analysis took place only for case B. The calibrated value was used for cases A and C

† Indicates that no sensitivity analysis took place because the phenomenon was not considered

× The first brackets contain the values for the kinematic viscosity in the domain, while the second brackets the values range for the viscosity sponge

Table 5: Calibrated SWAN-Thetis numerical configuration details for each of the examined test cases

		Longuet-Higgins and Stewart (1964)	Boers (1997)			Roelvink and Reniers 1995	Lai et al. 1989	Dingemans 1987
			Exp. A	Exp. B	Exp. C			
Thetis	Nodes	413		1981		1560	1044	914
	Elements	824		3960		3118	2086	1826
	Degrees of Freedom (DoF)	2256		11124		8556	5928	5178
SWAN	Nodes in xy-space	337		1470		109	1198	677
	No of frequencies	38		38		38	44	38
	Nodes in θ-space	5		11		21	6	6
Coupled model	Simulation time [min]	30		30		30	30	30
	Convergence time [min]	2.00	3.83	3.75	3.50	3.00	3.67	9.50
	CPU time [min]	2.98	3.75	3.77	3.80	7.60	2.75	4.21

*All the simulations were run serially in Linux x86_64 GNU/linux system equipped with 8 CPU (2 threads each) and an Intel Core i7 with 32GB RAM.

flume's bottom was composed of sand with a smooth concrete layer finish. Three wave conditions, described by their significant wave height H_s and their peak period T_p, were applied: (a) $H_s = 0.16$ m and $T_p = 2.1$ s; (b) $H_s = 0.22$ m and $T_p = 2.1$ s; and (c) $H_s = 0.10$ m and $T_p = 3.4$ s (Table 2) with normal incident wave direction towards the shore.

The numerical domain representing the experimental setup consists of the nested setup shown in Fig. 3b encompassing a subdomain of 45 m in length and 5 m in width in the area of interest D_2. The bathymetry is constant in the y-direction and ranges from 0.05 m to 0.80 m in x-direction (Fig. 3b). The mesh employed by SWAN is uniformly structured in both directions with $dx = dy = 0.4$ m, while the mesh in Thetis retains an element length of 0.4 m (Table 3).

The wave boundary condition is applied to the left boundary of SWAN with direction perpendicular to the shore located at the right (E) of the domain. Similarly for Thetis, the measured water elevation is imposed on the left (W) boundary, while a no-slip condition is applied at the shore. Finally, the top (N) and bottom (S) boundaries are described by a free-slip condition mimicking smooth surfaces typical of lab-scale experiments (Table 2).

Bed friction losses in SWAN are accounted for by employing the Madsen formulation (Madsen et al., 1989) with roughness length scale $k_n = 0.02$ m, while no bed friction effects are included in Thetis. In addition, depth-induced wave-breaking is considered with $\alpha_{BJ} = 1.5$ and $\gamma = 0.63$, whereas no wind input is accounted. The implicit nature of SWAN's propagation scheme allows the employment of a timestep $dt_{SWAN} = 10$ s and considering the semi-implicitness of Thetis' numerical scheme a smaller timestep $dt_{Thetis} = 5$ s is considered.

3.3. Roelvink and Reniers (1995) case on wave-induced undertow current

As part of the EU Large Installations Plan framework (LIP11D) Roelvink and Reniers (1995) examined the phenomenon of a sandbar formation and migration caused by wave-induced undertow current in a large-scale flume with length 225 m, width 5 m and depth 7 m. During the experiment three wave conditions were applied resulting in different beach states. We select the first one comprised of narrow-banded irregular waves of $H_s = 0.95$ m and $T_p = 5$ s traversing perpendicular to the shore generating a stable beach.

To numerically reproduce the experiment, the nested domain shown in Fig. 3c is implemented. The bathymetry ranges from $h = 0.20$ m to $h = 4.10$ m; specifically in the first 20 m the bathymetry is flat with $h = 4.10$ m, followed by a constant 1:20 slope until $x = 52$ m, after which the still water depth adheres to a power function $h\,(x) = 0.1\,(177 - x)^{2/3}$ till $x = 169$ m, resulting to a 1:30 slope. The uniform structured mesh in SWAN has a resolution of 5.0 m, while Thetis mesh resolution is $\wedge h = 0.5$ m nearshore and $\wedge h = 2.5$ m at deep water.

Regarding the boundary conditions (Table 2), the forcing boundary conditions are imposed on the left boundary; the wave boundary condition in SWAN and the known water elevation in Thetis. Similarly to the previous two cases, bottom friction has been accounted in SWAN with Madsen's $k_n = 0.05$ m, in addition to the implementation of depth-induced wave-breaking dissipation with $a_{BJ} = 1.0$ and $\gamma = 0.73$. In Thetis, only wetting and drying has been included with $\alpha_{wd} = 2.5$ m. Both models utilise the same timestep $\Delta t_{\text{SWAN}} = \Delta t_{\text{Thetis}} = 3$ s, which is also the coupling timestep (Table 3).

3.4. Lai et al. (1989) case on a strong opposing current

The blocking of waves, breaking or non-breaking, caused by an opposing current was studied in the experiment of Lai et al. (1989) in a tank with a 18.3 m long, 0.91 m wide and 1.22 m deep test section. The waves were generated by the wave-maker located at the left (W) side of the tank, while a current was imposed through a pump on the opposite side. We focus on a monochromatic wave described by $H_s = 0.019$ m and $T_p = 0.57$ s travelling from left (W) to right (E), while the current's speed starts at 0.13 $\mathrm{m\,s^{-1}}$ evolving to approximately 0.22 $\mathrm{m\,s^{-1}}$ over the bar.

The numerical domain for this setup is presented in Fig. 3d. The domain of interest D_2 has 28 m length, 10 m width and the water depth ranges from 0.45 m to 0.75 m. The structured mesh utilised in SWAN is uniform with mesh spacing 0.5 m , while the Thetis mesh element length varies from $\wedge h = 0.4$ m on the top of bar radially increasing to $\wedge h = 1.0$ m at the forcing boundaries. These boundaries entail a current entering the domain on the right (E) which is assigned a magnitude of 0.13 $\mathrm{m\,s^{-1}}$ that leaves on the left (W) of the domain. This is imposed in Thetis alongside the wave conditions in SWAN (Table 2). The effect of depth-induced wave-breaking and bottom friction are absent, along with the negligible contribution of whitecapping dissipation. Similarly, in Thetis neither wetting and drying nor bed shear stress are included (Table 3).

3.5. Dingemans (1987) 2-D setup on waves over a submerged bar

The experiment of Dingemans (1987) consists of a semi-cylindrical submerged bar with bathymetry ranging from 0.10 m to 0.40 m in a flume 30 m long and 26.4 m wide. Alongside the left side of the flume is a wave-generator, while on the opposite site a wave-absorbing beach was constructed with a 1:7 slope. The bathymetry follows a 1:20 slope on the left bank of the bar and 1:10 on the right. Dingemans (1987) implemented a plethora of wave conditions; the focus on this study falls on the case with a JONSWAP spectrum (Hasselmann et al., 1973) described by $H_s = 0.10$ m and $T_p = 1.25$ s. During the experiments the water velocities were recorded through 81 current gauges placed on a 3 m $\times$ 3 m grid, in addition to the water elevations captured by the wave gauges (Fig. 3f).

The numerical domain utilised here (Fig. 3e) follows Dingemans (1987) bathymetry, but has extended the submerged bar a further 20 m to calculate accurately wave boundary conditions for domain D_2 and to minimise boundary errors. SWAN and Thetis meshes employ the same 2 m resolution, the former in a uniform structured grid and the latter in terms of mesh element length. The known wave boundary condition is applied on the left boundary, while we emulate

Table 6: Definition of statistical parameters

Name	Notation	Formula	Meaning
Goodness-of-fit	R^2	$R^2 = 1 - \frac{\sum_i^n (y_i - \hat{y}_i)^2}{\sum_i^n (y_i - \overline{y})^2}$	Degree of linear correlation to the fit $y_i = 1 \cdot \hat{y}_i + 0$
Pearson correlation coefficient	r	$r = \frac{\sum_i^n (y_i - \overline{y})(\hat{y}_i - \overline{\hat{y}})}{\sqrt{\sum_i^n (y_i - \overline{y})^2 \sum_i^n (\hat{y}_i - \overline{\hat{y}})^2}}$	Measures linear correlation between observed and predicted values
Root Mean Square Error	r.m.s.e.	$\text{r.m.s.e.} = \sqrt{\frac{\sum_i^n (y_i - \hat{y}_i)^2}{n}}$	Quantifies concentration level around the best fit line.
Mean Absolute Error	m.a.e.	$\text{m.a.e.} = \frac{\sum_i^n \lvert y_i - \hat{y}_i \rvert}{n}$	Average magnitude error between predictions and observations.
Bias	*bias*	$bias = \frac{\sum_i^n y_i - \hat{y}_i}{n}$	Deviation of predicted values from equivalent observations. If linear correlation $y_i = 1 \cdot \hat{y}_i + 0$ is the best fit, $bias = 0$.
Willmott index (Willmott, 1981)	d	$d = 1 - \frac{\sum_i^n (y_i - \hat{y}_i)^2}{\sum_i^n (\lvert \hat{y}_i - \overline{y} \rvert + \lvert y_i - \overline{y} \rvert)^2}$	Measures distance between predicted and observed values.

* where n is the size of the dataset; y_i are the observed values; $\hat{y}_i$ are the predicted values; $\overline{y}$ is the mean of the observed values; and $\overline{\hat{y}}$ is the mean of the predicted values

the wave absorbing beach on the right side through a no-slip condition (Table 2). Bed friction losses have been accounted in SWAN per Madsen's formulation with $k_n = 0.04$ m and in Thetis following the Manning formulation with $n_M = 0.022$. Depth-induced wave-breaking has also been considered with $a_{BJ} = 1$ and $\gamma = 0.73$, while no wind input is implemented. SWAN's implicit scheme allows for a relatively big timestep of 60 s, while Thetis utilises a much shorter timestep $dt_{\text{Thetis}} = 1$ s (Table 3).

4. Results

A synoptic table (Table 3) containing the "default" and calibrated values of the parameters examined in sensitivity analyses for all cases is included alongside a table depicting the computational details, including simulation, convergence and CPU time, for each test case (Table 5). The final configuration is compared against the analytical solution or experimental data, its performance assessed through a series of statistical parameters (Table 6). When available, a cross-comparison between our model's and other models' predictions, found in literature, is presented through infographics and statistical quantities. The numerical configuration of the literature models is collated in Table 7.

4.1. Longuet-Higgins and Stewart (1964) case on wave set-up on a linearly sloped beach

This setup has specifically been employed by Roland et al. (2012) (dashed green line, Fig. 4) and Xia et al. (2004) (blue dashed line, Fig. 4b) to validate their models; the former with regards to their developed coupled model and the latter as per the implementation of a new vertical profile extension of the radiation stress (for details of their numerical setup, see Table 7). Our calibrated setup prediction for water elevation η (continuous red line, Fig. 4) verges on an exact match of the analytical solution of Longuet-Higgins and Stewart (1964) (continuous

Table 7: Numerical model setup for studies in the literature regarding the validation cases of Table 1

Model	Length (x-direction), L_x [m]	Width (y-direction), L_y [m]	Depth (z-direction), L_z [m]	Mesh resolution in x-direction, dx [m]	Mesh resolution in y-direction, dy [m]	Mesh resolution in z-direction, dz [m]	Coupling timestep $dt_{coupling}$ [s]	Ocean model timestep, dt_{ocean} [s]	Wave model timestep, dt_{wave} [s]	Simulation time [min]	Convergence time [min]	CPU time [min]
Longuet-Higgins and Stewart 1964												
Roland et al. 2012	9.0	-*	0.45	0.125	0.125	0.05	0.05	0.05	¡ 0.05	60	$\sim$ 36	-*
Xia et al. 2004	9.0	-*	0.45	0.125	-*	0.125	0.002	-*	-*	-*	-*	-*
Boers 1997												
Roland et al. 2012	28.5†	-*	0.80	0.05	0.05	0.089	0.1	0.1	-*	-*	$\sim$ 22	-*
Marsooli et al. 2017	28.5†	-*	0.80	0.1	0.1	0.05	0.005	0.005	0.0025	30	-*	-*
Roelvink and Reniers 1995												
Marsooli et al. 2017	175	-*	4.10	1.0	1.0	0.205	0.01	0.01	0.005	60	-*	-*
Lai et al. 1989												
Roland et al. 2012	7.925†	-*	0.75	0.02	2.0	0.125	0.1	-*	-*	10	$\sim$ 7	-*
Ris and Holthuijsen 1996	9.0†	-*	0.75	-*	-*	N/A	N/A	N/A	N/A	N/A	N/A	-*
Dingemans 1987												
Roland et al. 2012	25†	28†	0.4	[0.20, -*]		0.44	0.5	0.5	-*	$\sim$ 42	$\sim$ 13.5	-*

*: The value was not reported

†: Values inferred from model predictions figures

Table 8: Model performance against the analytical solution of the Longuet-Higgins and Stewart (1964) setup by statistical quantities of Table 6

Variable	Model	R^2 [-]	r [-]	r.m.s.e [m]	m.a.e [m]	*bias* [m]	d [-]
H	Roland et al. (2012)	0.998	1.000	0.001	0.001	-0.001	1.000
	SWAN-Thetis (def.)	0.896	0.984	0.009	0.005	-0.001	0.964
	SWAN-Thetis (cal.)	0.940	0.982	0.007	0.003	0.000	0.982
η	Roland et al. (2012)	0.896	0.999	0.003	0.003	-0.002	0.970
	Xia et al. (2004)	0.837	0.979	0.003	0.003	-0.001	0.941
	SWAN-Thetis (def.)	0.828	0.983	0.003	0.002	0.001	0.934
	SWAN-Thetis (cal.)	0.988	0.994	0.001	0.000	0.000	0.997

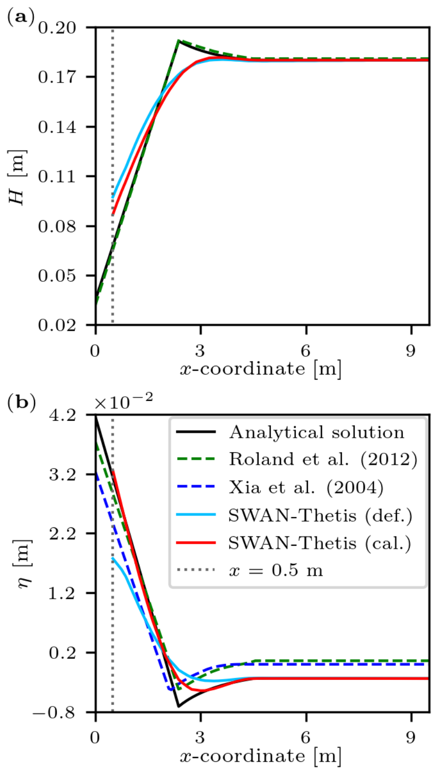

Figure 4: (a): Profile of wave height H; and (b) water elevation η profile for the Longuet-Higgins and Stewart (1964) setup

black line, Fig. 4b) excluding the area of wave-breaking (2 m $\leq x \leq$ 3 m) resulting in goodness-of-fit $R^2 = 0.99$ (Table 8). Despite the lower R^2 of the literature models (Roland et al., 2012; Xia et al., 2004), they capture better the shape of η profile during wave-breaking despite their over-estimation of η offshore and its under-estimation closer to the shore (Fig. 4b).

On the wave height H, Roland et al. (2012) reproduced Longuet-Higgins and Stewart (1964) analytical solution with $R^2 = 1$ (Fig. 4a, Table 8). As we do not reproduce the abrupt transition due to wave-breaking (2 m $\leq x \leq$ 4 m) in addition to a slight overestimation of H afterwards, R^2 is smaller $\left(R^2 = 0.94,\ \text{Table 8}\right)$.

Table 9: Model performance against data from the Boers (1997) experiments by statistical quantities of Table 6

Variable	Model	R^2 [-]	r [-]	r.m.s.e [m]	m.a.e [m]	*bias* [m]	d [-]
Experiment A							
H_s	Roland et al. (2012)	0.961	0.988	0.007	0.006	-0.001	0.991
	SWAN-Thetis (def.)	0.935	0.978	0.009	0.007	-0.003	0.981
	SWAN-Thetis (cal.)	0.936	0.981	0.009	0.007	-0.003	0.981
η	Roland et al. (2012)	0.439	0.932	0.002	0.002	-0.002	0.891
	SWAN-Thetis (def.)	0.726	0.888	0.001	0.001	0.000	0.903
	SWAN-Thetis (cal.)	0.746	0.895	0.001	0.001	0.000	0.909
Experiment B							
H_s	Roland et al. (2012)	0.979	0.993	0.007	0.005	0.001	0.995
	Marsooli et al. (2017)	0.980	0.993	0.007	0.006	-0.004	0.995
	SWAN-Thetis (def.)	0.922	0.994	0.013	0.010	-0.009	0.977
	SWAN-Thetis (cal.)	0.961	0.987	0.009	0.008	-0.003	0.989
η	Roland et al. (2012)	0.641	0.955	0.002	0.002	-0.002	0.922
	Marsooli et al. (2017)	0.800	0.961	0.002	0.001	-0.001	0.951
	SWAN-Thetis (def.)	0.818	0.942	0.002	0.001	0.000	0.934
	SWAN-Thetis (cal.)	0.775	0.913	0.002	0.001	-0.001	0.926
Experiment C							
H_s	Roland et al. (2012)	0.768	0.922	0.011	0.009	0.006	0.943
	Marsooli et al. (2017)	0.872	0.979	0.008	0.007	-0.004	0.958
	SWAN-Thetis (def.)	0.615	0.948	0.014	0.011	0.005	0.821
	SWAN-Thetis (cal.)	0.741	0.937	0.011	0.009	-0.001	0.892
η	Roland et al. (2012)	-0.907	0.858	0.002	0.001	-0.001	0.753
	Marsooli et al. (2017)	0.783	0.977	0.001	0.001	0.000	0.961
	SWAN-Thetis (def.)	0.730	0.939	0.001	0.001	0.000	0.885
	SWAN-Thetis (cal.)	0.764	0.910	0.001	0.001	0.000	0.918

4.2. Boers (1997) case on surf zone with a barred beach

This experiment has been a popular validation case among wave-current interaction coupled models (see Roland et al. (2012) and Marsooli et al. (2017)). Roland et al. (2012) (dashed blue line, Fig. 5) utilised all three wave conditions (Table 2) and Marsooli et al. (2017) only the last two (dashed green line, Fig. 5c-f). Even though Roland et al. (2012) utilises a 3-D model, our calibrated 2-D setup (continuous red line, Fig. 5) simulates η better, as the former over-estimates η near and after wave-breaking ($x \geq 20$ m) (Fig. 5b,d,f). This is also confirmed by the superior values of R^2 for "SWAN-Thetis (cal.)" with $R^2 \approx 0.76$ compared to R^2 ranging from -0.91 to 0.64 for Roland et al. (2012). Furthermore, for wave conditions A and B sharing $T_p = 2.1$ s, the significant wave height H_s predictions of our calibrated model are more fitting to the observed values (black dots, Fig. 5a,c) in intermediate waters (5 m $\leq x \leq$ 16 m) in comparison to the other models exhibited.

On the other hand, models in the literature simulate with more precision H_s nearshore ($x \geq 20$ m in Fig.5a,c,e; Table 9). This superior performance nearshore is also exhibited in η (Fig. 5b,d,f), since Roland et al. (2012) and Marsooli et al. (2017) capture the shape of η profile more accurately, even though they generally overestimate it. This behaviour is expressed through the higher values of the Pearson correlation coefficient r in conjunction with the lower, for Roland et al. (2012), or equivalent, for Marsooli et al. (2017), R^2 (Table 9) compared to our calibrated results.

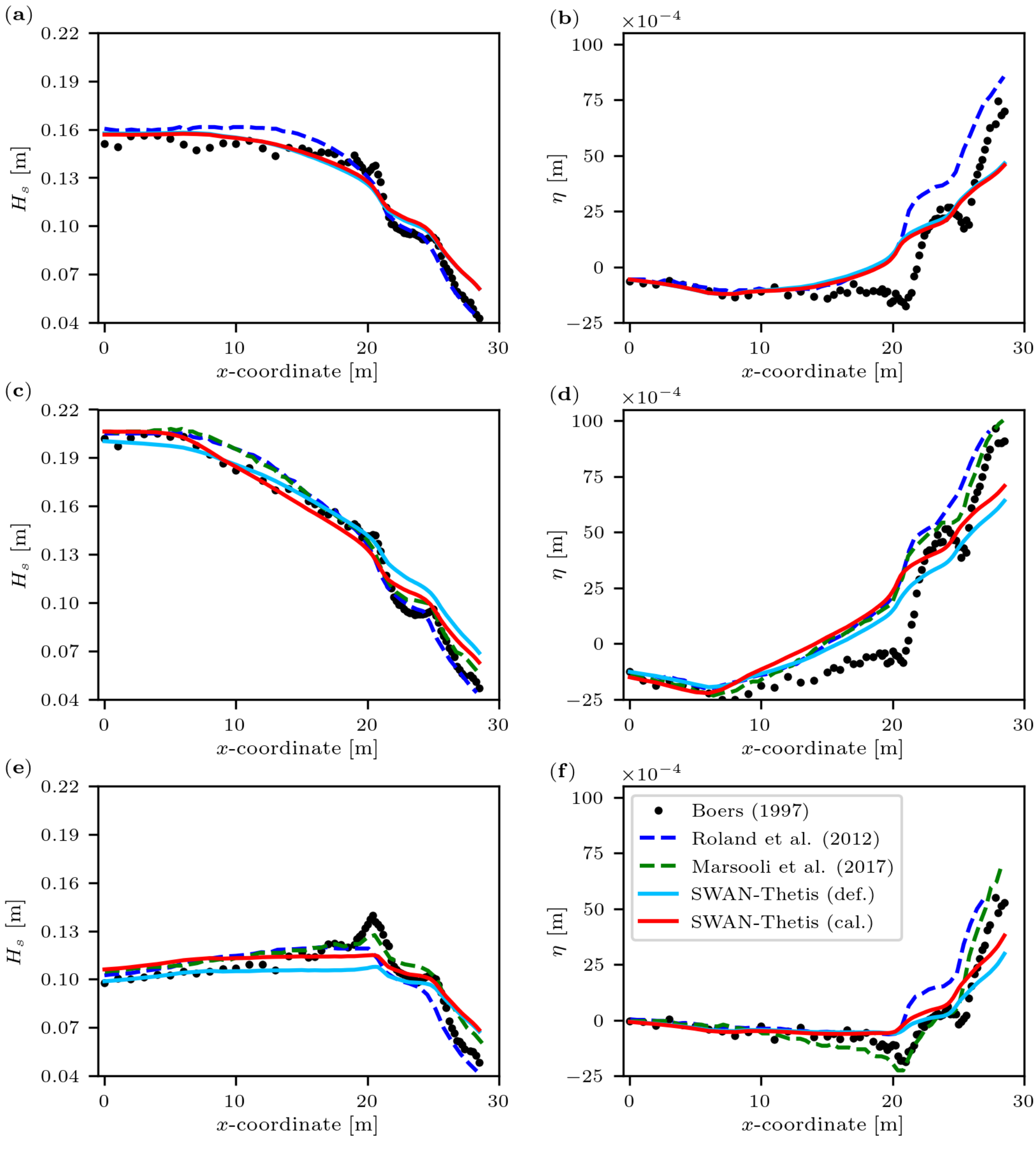

Figure 5: Left column: Significant wave height H_s profile across the domain depicted in Fig. 3b for wave conditions A, B, and C, respectively. Right column: Water elevation η profile in the Boers (1997) experiment for wave conditions A, B, and C, accordingly.

4.3. Roelvink and Reniers (1995) case on wave-induced undertow current

The Roelvink and Reniers (1995) experiment was studied to evaluate the model ability of Marsooli et al. (2017) to simulate wave-induced undertow currents. Firstly, Marsooli et al.

(2017) (dashed blue line, Fig. 6) predicts more accurately the water elevation in waters of transitional depth (30 m $\leq x \leq$ 120 m); a drop in H_s is instead observed for our calibrated model results (continuous red line, Fig. 6). Nonetheless we provide a more accurate H_s prediction nearshore ($x \geq$ 150 m). Overall, comparable statistics (Table 10) are derived, with our model showing a marginally better performance. Concerning H_s, both models bear identical profiles in agreement with the observed values $\left(R^2 \approx 0.97\right)$ (black dots, Fig. 6a).

Table 10: Model performance against measurements from the Roelvink and Reniers (1995) experiment by the statistical quantities of Table 6

Variable	Model	R^2 [-]	r [-]	r.m.s.e [m]	m.a.e [m]	*bias* [m]	d [-]
	Marsooli et al. (2017)	0.974	0.989	0.033	0.028	-0.008	0.993
H_s	SWAN-Thetis (def.)	0.973	0.993	0.034	0.027	-0.021	0.993
	SWAN-Thetis (cal.)	0.979	0.992	0.030	0.022	-0.014	0.995
	Marsooli et al. (2017)	0.889	0.974	0.006	0.005	0.002	0.963
η	SWAN-Thetis (def.)	-0.240	0.981	0.021	0.016	-0.010	0.860
	SWAN-Thetis (cal.)	0.929	0.966	0.005	0.004	0.000	0.982

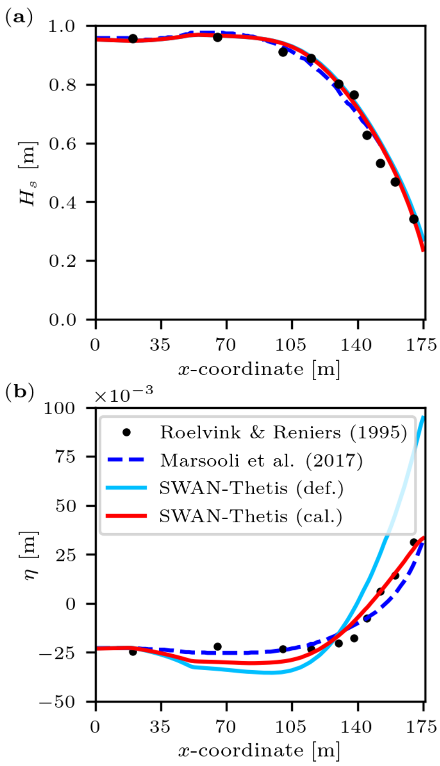

Figure 6: (a): Profile of significant wave height H_s; and (b) water elevation η profile for the Roelvink and Reniers (1995) case

4.4. *Lai et al. (1989) case on a strong opposing current*

The experimental investigation of Lai et al. (1989) has been previously considered by Roland et al. (2012) and Ris and Holthuijsen (1996). Although our model (continuous red line, Fig. 7a) deviates from other model results that simulate current-induced wave-breaking, as calculated by Roland et al. (2012) (green triangles, Fig. 7a) and Ris and Holthuijsen (1996) (dashed blue line, Fig. 7a), it exhibits the best overall $R^2 = 0.69$ (Table 11), as models in the literature over-predict H near the false bottom ($6\text{ m} \leq x \leq 11\text{ m}$). Even though our modelling exhibits the best statistical performance, the ineptitude to capture the reduced H after the bar is universal across all models.

On the current velocity u, our calibrated prediction (continuous red line, Fig. 7b) slightly underestimates the measured profile (continuous black line, Fig. 7b), even though a noticeable difference is seen due to the scale of the y-axis. Specifically, (i) the predicted velocity over the bar is 0.213 m s^{-1} against the measured 0.217 m s^{-1}; and (ii) the velocities near the bottom of the bar are marginally smaller, i.e. 0.125 m s^{-1} against the observed 0.13 m s^{-1}. These inconsistencies induce the small m.a.e. of 0.004 m s^{-1} and a Willmott index $d = 0.99$ (Table 11).

Table 11: Model performance against the experimental data of the Lai et al. (1989) setup by the statistical quantities of Table 6

Variable	Model	R^2 [-]	r [-]	r.m.s.e [*]	m.a.e [*]	*bias* [*]	d [-]
H	Roland et al. (2012)	0.486	0.888	0.004	0.004	-0.003	0.865
	Ris and Holthuijsen (1996)	0.653	0.938	0.004	0.003	-0.003	0.887
	SWAN-Thetis (def.)	0.244	0.840	0.005	0.004	-0.003	0.674
	SWAN-Thetis (cal.)	0.692	0.876	0.003	0.003	0.000	0.874
u	SWAN-Thetis (def.)	0.981	0.994	0.005	0.003	0.003	0.995
	SWAN-Thetis (cal.)	0.973	0.994	0.006	0.004	0.004	0.993

* The units are m for the wave height H and m s^{-1} for the current velocity u.

4.5. Dingemans (1987) 2-D setup on waves over a submerged bar

Roland et al. (2012) (black dots, Fig. 8) also made use of the experiment by Dingemans (1987) to validate their model performance with regards to the significant wave height H_s and the current velocities u, v in a 2-D setup. Their overestimation of the smaller H_s (for $H_s \leq 0.10$ m) results in a much lower R^2 $\left(R^2 = 0.59\right)$ compared to $R^2 = 0.89$ (Table 12) for our calibrated setup (red circles, Fig. 8a).

Similarly, we simulate the v-velocity with marginally more precision $\left(R^2 = 0.79\right)$ since Roland et al. (2012) tends to slightly under-estimate $-0.1\text{ m s}^{-1} \leq v \leq 0.1\text{ m s}^{-1}$ with $R^2 = 0.74$. Concerning the other component of current velocities, i.e. u (Fig. 8b), the models exhibit similar results in relative accordance to the measurements with $R^2 = 0.81$ and r.m.s.e $= 0.04\text{ m s}^{-1}$ (Table 12).

5. Discussion

5.1. Sensitivity analysis

An exploration of a series of parameters was performed through sensitivity analyses for each case study. The initial setup containing the "default" values is arranged alongside the calibrated model (Table 3) with the value range summarised in Table 4 for completeness.

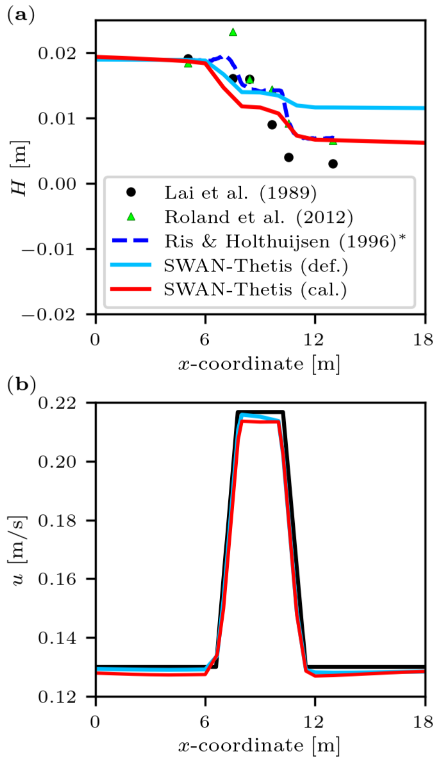

Figure 7: (a): Profile of wave height H; and (b) current velocity u profile for the Lai et al. (1989) setup

Table 12: Model performance against measurements from the Dingemans (1987) experiment by the statistical parameters of Table 6

Variable	Model	R^2 [-]	r [-]	r.m.s.e [*]	m.a.e [*]	*bias* [*]	d [-]
H_s	Roland et al. (2012)	0.590	0.912	0.011	0.008	-0.007	0.859
	SWAN-Thetis (def.)	0.731	0.898	0.009	0.007	-0.004	0.935
	SWAN-Thetis (cal.)	0.918	0.965	0.005	0.004	0.002	0.979
u	Roland et al. (2012)	0.819	0.910	0.043	0.032	-0.006	0.944
	SWAN-Thetis (def.)	0.199	0.859	0.090	0.067	0.011	0.373
	SWAN-Thetis (cal.)	0.810	0.927	0.044	0.035	-0.006	0.934
v	Roland et al. (2012)	0.738	0.876	0.035	0.027	0.010	0.915
	SWAN-Thetis (def.)	0.223	0.694	0.061	0.048	-0.013	0.503
	SWAN-Thetis (cal.)	0.791	0.910	0.031	0.024	0.004	0.928

* The units are m for the significant wave height H_s and m s^{-1} for the current velocities u, v.

5.1.1. Temporal and mesh convergence

The analysis commenced with the mesh resolution of SWAN (dx) and Thetis ($\wedge h$) assuming that the time-steps $\Delta t_{\text{SWAN}} = \Delta t_{\text{Thetis}} = 1$ s are small enough for the CFL condition to be met. Ordinarily, the coarser resolutions investigated (Table 4) yield insubstantial differences except when refraction is prominent (Roelvink and Reniers, 1995; Dingemans, 1987). The sensitivity

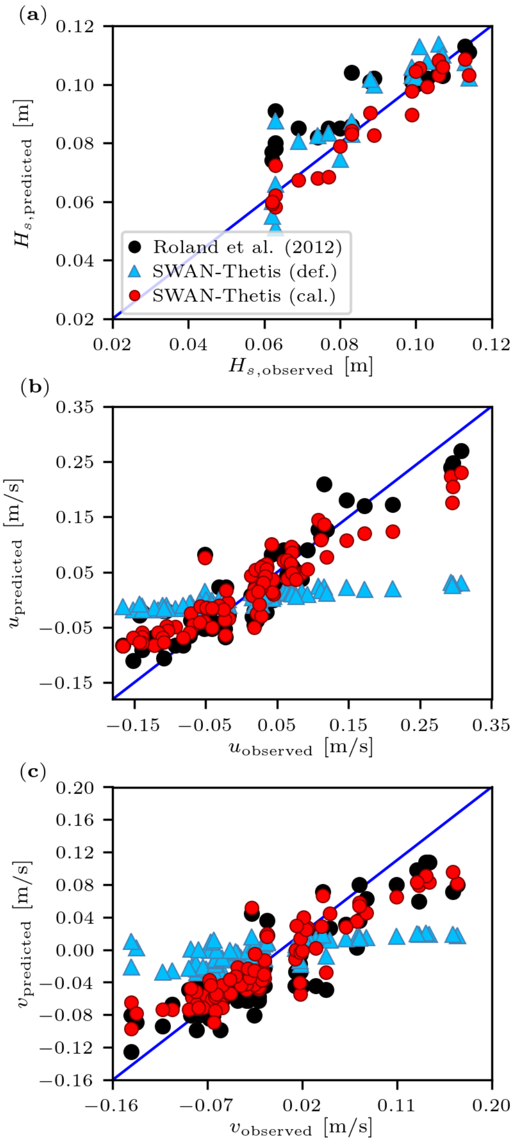

Figure 8: The observed (x-axis) against the predicted (y-axis) values for the Dingemans (1987) experiment for: (a) the significant wave height H_s, (b) the current velocity u; and (c) the current velocity v.

Table 13: Computational cost expressed as CPU time for the default and calibrated setup

Case	Default setup CPU time T_D	Calibrated setup CPU time T_C	$\frac{T_D}{T_C}$
Longuet-Higgins and Stewart (1964)	00:06:53	00:02:59	2.3
Boers (1997) (Exp. B)	00:40:27	00:03:46	10.7
Roelvink and Reniers (1995)	00:18:03	00:07:26	2.4
Lai et al. (1989)	00:51:22	00:02:45	18.7
Dingemans (1987)	03:12:56	00:04:13	45.8

of results accuracy to refraction in non-stationary simulations is a known SWAN issue (SWAN Team, 2019) here exhibited for smaller dx in the Dingemans (1987) cases (Table 4); there, the Lipschitz criterion is violated allowing the energy to travel over a number of directional bins (SWAN Team, 2019). Hence, the imposition of a Courant number limiter is necessary for accurate predictions, which is insufficient to resolve non-convergence issues for $dx \leq 2.5$ m in the Roelvink and Reniers (1995) case; this is another known issue of SWAN (Booij et al., 2004)) though the limiter restricts the problem locally. Lastly, in the Lai et al. (1989) case, larger $\wedge h$ values result to a poor representation of the bathymetry with the u-profile near the bar transforming to a shape resembling the letter Λ instead of the anticipated Π as resolution decreases (Table 4). Poor results nearshore with coarser resolution are also exhibited in the large-scale experiment of Roelvink and Reniers (1995). Hence in the last two aforementioned cases, an unstructured mesh is employed in Thetis utilising a finer resolution focused specifically in the area of interest.

The other resolution variables related to computational cost are the time-steps employed by the models, Δt_{SWAN} and Δt_{Thetis}. Considering that the ranges tested exhibited no apparent impact on the results, but immensely influenced the CPU and convergence time, their selection was made on the basis of limiting convergence duration. Imposing a limit on the convergence time of 5 min for the quasi-1-D cases (Longuet-Higgins and Stewart, 1964; Boers, 1997; Roelvink and Reniers, 1995; Lai et al., 1989) and 10 min for the Dingemans (1987) experiment, the time-step with the minimum CPU time conforming to this restriction is chosen (Table 3) resulting in relatively large time-steps for SWAN (generally $\Delta t_{\text{SWAN}} \geq 10$ s) and smaller time-steps for Thetis ($\Delta t_{\text{Thetis}} \leq 5$ s). SWAN's limitations on refraction resulting in non-convergence necessitated the change of SWAN's numerical scheme for refraction to a first-order upwind and a small time-step ($\Delta t_{\text{SWAN}} = 3$ s) in the Roelvink and Reniers (1995) experiment. Refraction's numerical scheme was also converted to a first-order upwind in the Dingemans (1987) experiment to decrease the convergence time. Additionally, for the model to converge within the specified time frame, ν was increased to 1 m^{2}s in Thetis. The time and mesh sensitivity analyses led to reduced CPU time requirement ranging from an acceleration of 2.3× for the idealised case of Longuet-Higgins and Stewart (1964) to 45.8× for the 2-D experiment of Dingemans (1987) (Table 13), substantially constraining the computational cost for the subsequent analyses.

5.1.2. SWAN parameters

Considering the monochromatic or narrow-band wave conditions implemented, the suggested directional standard deviation $\sigma_\theta = 30^o$ by SWAN (Booij et al., 2004) was not contemplated. Decidedly smaller σ_θ values are investigated (Table 4) with the majority of cases employing $\sigma_\theta \leq 3.5^o$ (Table 3). The relatively high $\sigma_\theta = 5^o$ in the case of Lai et al. (1989) is chosen to reduce the wave height providing more precise H predictions downstream of the bar, since it has been observed that higher values of the spreading index s or as denoted in SWAN m correspond to higher values of H (Venugopal et al., 2005), while m is negatively correlated with σ_θ (Holthuijsen, 2010; Booij et al., 2004).

On the bed losses, the shallow water depths dominating the Boers (1997) experiment require a decreased value from the suggested $k_n = 0.05$ m (Table 3) to avoid overestimating bed friction dissipation. This issue does not arise on the large-scale (Roelvink and Reniers, 1995) and the 2-D experiment (Dingemans, 1987) (0.04 m $\leq k_n \leq 0.05$ m) most likely due to the bathymetry resembling "regional" applications. No analysis is performed for the Longuet-Higgins and Stewart (1964) idealised setup as all phenomena except for depth-induced wave-breaking have been neglected.

Similar findings are observed for the parameters describing the depth-induced dissipation, α_{BJ} and γ. Specifically, Roelvink and Reniers (1995) and Dingemans (1987) employ the default values $\alpha_{BJ} = 1$ and $\gamma = 0.73$ to accurately represent the phenomenon. On the other hand, a slight adjustment of $\alpha_{BJ} = 1.5$ is crucial in the small scale setups (Longuet-Higgins and Stewart, 1964; Boers, 1997) due to dissipation under-estimation. On the breaker index, the analytical solution of Longuet-Higgins and Stewart (1964) considers $\gamma = 0.83$, confirmed by the investigation (Table 4) since smaller γ results in wave-breaking shifting towards deep waters. In the Boers (1997) experiment, $\gamma = 0.63$ and $\gamma = 0.73$ procure statistically similar predictions, with the former capturing better the second wave-breaking severely under-calculated by the latter. Considering the small wave height ($H < 0.02$ m) traversing the domain and the relative deep waters ($h \geq 0.45$ m) no depth-induced wave-breaking occurs in the Lai et al. (1989) experiment, verified by the analysis for α_{BJ} (Table 4, 3).

Lastly, in addition to the sensitivity summarised in Table 3, an investigation on of the high-frequency cut-off limit f_{max} was performed specifically for the Lai et al. (1989) case. f_{max} together with the low-frequency cut-off f_{min} define the spectrum's prognostic range ($f_{min} < f < f_{max}$) where energy density develops unrestricted and the diagnostic range ($f < f_{min}$ and $f > f_{max}$) where the wave-wave interactions at high frequencies and integral wave parameters are calculated (Holthuijsen, 2010). The "default" $f_{max} = 1$ Hz suggested for conditions at sea does not capture accurately wave-blocking. A range of $f_{max} = [1, 2]$ Hz was examined with higher f_{max} generating smaller H downstream the bar. However, for $f_{max} > 1.8$ Hz the model does not accurately capture H on the left side where the wave condition is imposed, most likely due to excluding significant frequencies from the diagnostic spectrum range. Hence, $f_{max} = 1.8$ Hz was employed to accurately account for wave-blocking conditions.

5.1.3. Thetis parameters

Moving on to the remaining Thetis parameters, apparent is the effect of eddy viscosity ν investigations on the cases where current measurements are provided (Lai et al., 1989; Dingemans, 1987). Considering how a constant eddy-viscosity turbulence modelling approach is imposed for simplicity, higher values of ν are accompanied by a decline in current magnitude due to the smoothing effect of the viscosity term. Consistently, smaller ν was encouraged to accurately predict wave-current interactions (Table 3). However, depending on the domain and the bathymetry, smaller ν could lead to convergence complications as exhibited in the test case of Boers (1997) where for $\nu \leq 0.25$ m^2 s the model failed to converge, while for the Roelvink and Reniers (1995) experiment this was observed for $\nu \leq 1$ m^2 s (Table 4). On the cases where only wave height and water elevation are examined (Longuet-Higgins and Stewart, 1964; Boers, 1997; Roelvink and Reniers, 1995) apart from a decrease on convergence time as ν escalates, the results remained constant. Thus, while low values of ν are recommended in low turbulence regions to minimise turbulent diffusion for accurate current predictions there is a constraint associated with the convergence. Finally, to eliminate any spurious oscillations in the boundaries resulting in our model diverging, a viscosity sponge is employed in the numerical setup of Roelvink and Reniers (1995).

The wetting and drying parameter α_{wd} modifies the bathymetry by shifting it downwards, the larger the α_{wd} the bigger the depth increase. Hence, considering the under-estimation of currents already present in the Dingemans (1987) case and the slight under-evaluation of u in the Lai et al. (1989) experiment, no wetting-and-drying is considered ($\alpha_{wd} = 0$) (Table 3, 4) lest the velocities decrease further. In the remaining cases, α_{wd} is proportional to the bathymetric range of each domain, with $\alpha_{wd} = 0.1$ m for the small setup of Longuet-Higgins and Stewart (1964) ($h \leq 0.45$ m) and $\alpha_{wd} = 0.5$ m for the Boers (1997) experiment ($h \leq 0.80$ m). A distinctively high value of 2.5 m considered in the undertow-current case (Roelvink and Reniers, 1995) is a result of the sensitivity analysis (Table 4). The undertow-current formulated by the waves and the bathymetry varies in depth; the top part travels shorewards and the bottom seawards, a behaviour not captured by a depth-averaged model. Hence, by considerably deepening the waters, a greater depth-averaged current is recovered that can represent the higher flow velocity near the surface interacting with the waves.

The manning coefficient n_M has virtually no effect on the results due to the small velocities (with magnitude ≤ 0.004 m s^{-1} for the Longuet-Higgins and Stewart (1964), Booij et al. (1999)

and Roelvink and Reniers (1995) case and $|U| \leq 0.217\ \mathrm{m\,s^{-1}}$ for the Lai et al. (1989) setup) in the quasi 1-D setups (Table 1). Its influence is only significant in the 2-D case (Dingemans, 1987), where bed shear stress $\boldsymbol{\tau_b}$ are generated in the submerged bar area affecting the velocities (Fig. 8b,c). The formation of $\boldsymbol{\tau_b}$ is facilitated by shallow waters and the decrease of η due to radiation stress. Hence, a decrease of n_M (Table 3) provides more accurate velocities on the bar, as the dissipation due to bottom friction is not being over-estimated. An influence on the results of Lai et al. (1989) was also expected, but for $n_M \leq 0.06$ (Table 4) the results were identical with negligible difference for $n_M = 0.060$. This behaviour is attributed to the small velocities in conjunction with the deep water conditions relative to the wave height.

5.2. Model cross-comparison observations

5.2.1. On the numerical implementation and computational cost

Computational cost is a critical aspect of numerical models. With CPU times under 5 min for the small setups and approximately 8 min for the large-scale experiment of Roelvink and Reniers (1995) (Table 5), our model has promising computational efficiency while linking both wave and current models. The coupled model competency is also demonstrated through its rapid convergence in its results; this is under 4 min for the quasi-1-D cases (Longuet-Higgins and Stewart, 1964; Boers, 1997; Roelvink and Reniers, 1995; Lai et al., 1989) and nearly 10 min for the sole 2-D setup (Dingemans, 1987). Equivalent information in the literature is scarce, with Roland (2008) documenting some convergence times but abstaining from any CPU times, while the other coupled models (Xia et al., 2004; Marsooli et al., 2017) do not expand on computational details, omitting in some cases the simulation times (Table 7). Based on convergence rates, our model converges faster than Roland et al. (2012); the ratio ranging from 1.4× for the Dingemans (1987) experiment to 18× for the idealised setup (Longuet-Higgins and Stewart, 1964), respectively.

Thetis semi-implicit numerical scheme alongside SWAN's implicit allow the employment of sufficient large time-steps, with SWAN utilising $\Delta t_{\mathrm{SWAN}} = [3, 60]$ s and Thetis $\Delta t_{\mathrm{Thetis}} = [1, 5]$ s resulting in coupling time-step $\Delta t_{coupling}$ ranging from 3 to 60 s (Table 3). The latter is at least 120× larger (Dingemans 1987 experiment) and utmost 10^4× larger (Xia et al. 2004 for the Longuet-Higgins and Stewart 1964 setup) than the coupling time-steps employed by the models we use for comparison (Table 7), though more iterations may be required by our model constituents to reach the subsequent time-step. Furthermore, the schemes applied in the coupled model support coarser meshes with the same level of accuracy in the results, with SWAN structured mesh resolution being 3.2× to 25× coarser than the mesh applied in the other coupled models (Table 3,7). The unstructured nature of Thetis mesh permits resolution refinement only in the area of interest without needlessly increasing the computational cost, such as in the Roelvink and Reniers (1995) setup where $\wedge h = 0.5$ m was employed nearshore with $\wedge h = 2.5$ m near the deep waters (Table 3) compared to the constant 1 m resolution of Marsooli et al. (2017) (Table 7). Therefore, the combination of larger timesteps, coarser mesh resolution and local refinement could culminate in a substantial reduction of computational resources compared to the existing coupled models.

5.2.2. On the depth-induced wave-breaking and wave setup

On depth-induced wave-breaking investigation in small scales (Longuet-Higgins and Stewart, 1964; Boers, 1997) our water elevation prediction η is more accurate than Roland et al. (2012) and Xia et al. (2004), when applicable. In the idealised setup (Longuet-Higgins and Stewart, 1964) this is attributed to their models applying $\eta \approx 0$ m as boundary condition instead of the calculated one in the ocean model (Fig. 4b) leading to $R^2 \leq 0.90$ against $R^2 = 0.99$ for our calibrated setup (Table 8). On the experimental study of Boers (1997), superior performance against Roland et al. (2012) $\big(R^2 \approx 0.76$ opposed to $-0.91 \leq R^2 \leq 0.64;$ Table 9$\big)$ lies in the overestimation of η nearshore from the latter (Fig. 5b,d,f), most likely as a consequence of the different formulations employed for the calculation of radiation stress. Roland et al. (2012) implement a simplified formulation of Longuet-Higgins and Stewart (1962) without accounting for any other wave-induced effect, while we introduce wave roller effects alongside the formulation of Mellor (2015).

Although statistically the cross-model performance for H is comparable in the Longuet-Higgins and Stewart (1964) setup (Table 8), we do not capture the sharp peak of wave-breaking (Fig. 4a) presumably due to SWAN's inability to represent such acute crests to avoid introducing instabilities. Another reason could lie in the coupled model framework which assumes parallel computations by default; even when the coupled model is run on a single core, SWAN assumes that it runs in parallel with one core, disabling some of its functionality supported solely in serial (Booij et al., 2004). One such commands is the inclusion of wave setup. Such differences are not observed in the Boers (1997) experiment with both Roland et al. (2012) and SWAN-Thetis exhibiting similar H_s profiles and statistical parameters (Fig. 5a,c,e; Table 9) attributed to both models employing the JONSWAP spectrum. The difference in spectrum could explain the superior performance of Marsooli et al. (2017) in wave condition C (Fig. 5e) with $R^2 = 0.87$ (Table 9) capturing the peaks representing wave-breaking, since they utilised the Donelan et al. (1985) spectrum. The distinct features among models, notably between SWAN-Thetis and Roland et al. (2012), become apparent in the adjustments utilised to accurately capture depth-induced wave-breaking dissipation. Roland et al. (2012) adjusted their depth-induced wave-breaking parameters by decreasing α_{BJ} from 1.0 to 0.5 and increasing γ to 0.8 from 0.73 to refrain from over-dissipation. In comparison, we increased the rate of dissipation α_{BJ} to 1.5 and decreased the breaker index to 0.63 (Table 3). This disparity is attributed to the different numerical schemes employed by the models.

5.2.3. On the large-scale experiment

Progressing on the Roelvink and Reniers (1995) experiment, even though the models have almost identical H_s profiles (Fig. 6a) and similar statistics for η (Table 10), their η predictions are quite distinct pertaining to the wave-induced undertow current leading to sandbar formation. The 3-D nature of Marsooli et al. (2017) recognises the early influence of waves on currents ($x \geq 60$ m) thus exhibiting more precision in the intermediate waters while nearshore they are under-predicting the gradient of η nearshore (Fig. 6b). The greater performance of our model emanates from the distinctively high value of the wetting-and-drying parameter $\alpha_{wd} = 2.5$ m to accurately capture the 3-D nature of undertow-current with depth-averaged velocities. Thus, a tremendous adjustment of the bathymetry is fundamental for our satisfying performance, easily corroborated by the η profile of our "default" setup (see "SWAN-Thetis (def.)", Fig. 6b).

5.2.4. On the strong opposing current

Having verified the effects of waves on currents, we investigate our ability to capture the effects of currents on waves through the experiment of Lai et al. (1989). Though the case has also been utilised by another coupled model (Roland et al., 2012), only energy spectra for the wave gauges' location (Fig. 3d) have been provided, which were converted to wave height following $E = \frac{1}{16}\rho g H^2$ for easier comparison with the other models results. Due to the observation scarcity, it is ambiguous if the waves break, reflect as a result of the bar or are weakened by the current. Hence, our uniqueness in not predicting an increased H near the bar's top does not indicate an error. Specifically, Ris and Holthuijsen (1996), who although not employing a coupled model, exploited this experiment to validate SWAN's whitecapping formulation (dashed blue line, Fig. 7a) do comment on the peculiarity of the elevated H in that location, since they expected a reduction of H.

5.2.5. On the 2-D configuration

We conclude with the exclusive 2-D experiment (Dingemans, 1987) where the calibrated setup achieves 1.54× more accurate H_s predictions than Roland et al. (2012) with $R^2 = 0.92$ to opposed to $R^2 = 0.59$, respectively (Table 12). Though our model favours smaller H_s compared to Dingemans (1987), the differences are small ranging from -11.25% to 14.73% with mean at -2.12% and s.d.error 5.65%. In contrast, Roland et al. (2012) over-estimates extensively $H_s \leq 0.1$ m, values which are located on the top and at the right of the bar with differences $\Delta H_s/H_{s,obs} = [-3.74, 44.44]\,\%$ with 10.63% mean and 12.44% s.d. error. Hence, our model appraises the depth-induced wave-breaking dissipation and refraction more appropriately than Roland et al. (2012). On the currents performance, we accurately capture the flow pattern with some discrepancies in the magnitude. Though both models exhibit comparable current predictions by over-estimating the smaller velocities and under-estimating the higher ones (Fig. 8b,c), these differences are slightly amplified in our model. The current travels faster on the top of the bar as a consequence of the elevated bathymetry and the decreased water level courtesy of radiation stress, while the smaller velocities occur on the north side of the bar (8 m $\leq x \leq$ 20 m, 17.5 m $\leq x \leq$ 25 m ; Fig. 3f). The culpability lies with the imprecise calculation of bed shear stress; virtually zero except at the area of the bar. By implementing a varying manning coefficient field these predictions could be improved, as a smaller n_M value assigned to the elevated bottom would consider the effects of waves on currents curtailing the bed shear stress miscount.

5.3. Limitations, extensions and prospective applications

Considering the coupled framework's structure, some limitations are inherent by the model constituents, such as SWAN's inability to calculate wave characteristics for really shallow water depths and to resolve refraction in non-stationary or large application. Others stem from the use of Thetis in its 2-D form, where depth-averaged velocities are unable to capture 3-D phenomena such as an undertow current. Furthermore, the implementation of recommended (i.e. "default") parameters could potentially lead to erroneous predictions as showcased by Section 5.1. Hence, calibration on both models is required.

Despite these constraints, the coupled model presents several advantages. The minimal modification required for the coupling at source code level maintains the models' flexibility by supporting the further independent development of Thetis and SWAN. These improvements can be easily and almost effortlessly included in the coupled framework. In addition, the implementation of BMI facilitates the interoperability of either the coupled framework or the model components on their own with other models employing BMI. Hence, we align with the goal set by the Community Surface Dynamics Modeling System (CSDMS) to promote a flexible, inter-operable and continually developing research software ecosystem (Tucker et al., 2021). Although not explicitly presented here, parallel implementation of the model is supported reducing significantly the CPU time. Lastly, the combination of the numerical schemes employed by the model combined with the 2-D nature of Thetis promote computational efficiency while maintaining the same levels of accuracy presented in 3-D wave-current interactions coupled models. Hence, our coupled framework presents opportunities to support optimisation studies (Clare et al., 2022), which include iterative simulations, adjoint modelling or data assimilation techniques (Warder et al., 2022; Funke et al., 2014).

This work paves the way to practical applications regional scales. A practical example within the coastal ocean domain relates to marine energy such as at the Orkney-Shetland archipelagos where both wave and tidal sites have already been leased (Johnson et al., 2012). Earlier efforts have demonstrated the simulation and optimisation of tidal energy systems (Jordan et al., 2022; Pennock et al., 2022) in the region, but considering the highly energetic wave conditions the optimisation approaches that embed broader metocean conditions would be invaluable.

6. Conclusions

A coupling between SWAN and Thetis models to account for wave-current interactions occurring by the co-existence of wave and current flows has been developed. SWAN is a 3rd-generation spectral wave model (Booij et al., 1999), while the 2-D configuration of the shallow-water equation model Thetis is utilised (Kärnä, 2020). A Python interface implemented through Basic Model Interface (Hutton et al., 2020) facilitates the coupling with minimal intrusion in the refactored source code. The different grids and time-steps employed by the model components allow greater flexibility. The two models run consecutively communicating internally when exchanging the necessary parameters. These are the significant wave height, mean wave direction, mean wavelength and percentage of wave-breaking calculated by SWAN necessary for calculating radiation stress and wave roller effects performed by Thetis, while Thetis provides water elevation and currents information.

A suite of benchmarking cases for wave-current interaction models, consisting of analytical and experimental scenarios in quasi 1-D and 2-D configurations, has been established. Their implementation by the coupled SWAN-Thetis framework successfully demonstrates its ability to represent wave-current phenomena. Specifically, its capability to account for depth-induced wave-breaking, wave setup, the effects of strong opposing currents in 1-D and 2-D configurations has been investigated. Through a systematic analysis, calibration discrepancies between the recommended values are acknowledged and explained, highlighting the necessity of calibration when wave-current interactions are prominent. Some of the parameters showcasing such differences are the friction coefficient employed by either model, the depth-induced wave-breaking parameters, as well as Thetis eddy viscosity. Our agreement with the data is strong for the calibrated setups and often on the same level of accuracy as other 3-D wave-current interaction models; this also entails less computational cost, as our model converges faster and requires less CPU time compared to other options.

CRediT authorship contribution statement

Anastasia Fragkou: Conceptualisation, Methodology, Formal analysis, Investigation, Validation, Software, Visualisation, Writing - original draft, Writing - review & editing. **Christopher Old:** Supervision, Writing - review & editing, **Vengatesan Venugopal:** Writing - review & editing, **Athanasios Angeloudis:** Conceptualisation, Writing - review & editing, Supervision, Funding acquisition

Acknowledgments

A. Fragkou acknowledges the support of University of Edinburgh through a School of Engineering PhD scholarship. A. Angeloudis acknowledges the support of the NERC Industrial Innovation fellowship grant NE/R013209/2. A. Angeloudis and C. Old acknowledge the support of the EC H2020 ILIAD DTO project under grant agreement 101037643.

References

Avdis, A., Candy, A.S., Hill, J., Kramer, S.C., Piggott, M.D., 2018. Efficient unstructured mesh generation for marine renewable energy applications. Renewable Energy 116, 842–856. URL: https://doi.org/10.1016/j.renene.2017.09.058, doi:10.1016/j.renene.2017.09.058.

Balay, S., Abhyankar, S., Adams, M., Brown, J., Brune, P., Buschelman, K., Dalcin, L.D., Dener, A., Eijkhout, V., Gropp, W.D., 2019. PETSc Users Manual .

Blumberg, A.F., Mellor, G.L., 1987. A description of a three-dimensional coastal ocean circulation model. Three-dimensional coastal ocean models 4, 1–16.

Boers, M., 1997. Simulation of a surf zone with a barred beach; part 1: wave heights and wave breaking. Oceanographic Literature Review 4, 292.

Booij, N., Haagsma, I.G., Holthuijsen, L.H., Kieftenburg, A.T.M.M., Ris, R.C., van der Westhuysen, A., Zijlema, M., 2004. SWAN Cycle III Version 41.31AB Users Manual , 118URL: https://swanmodel.sourceforge.io/download/zip/swanuse.pdf.

Booij, N., Ris, R.C., Holthuijsen, L.H., 1999. A third-generation wave model for coastal regions 1. Model description and validation. Journal of Geophysical Research: Oceans 104, 7649–7666. doi:10.1029/98JC02622.

Brown, J.M., 2010. A case study of combined wave and water levels under storm conditions using WAM and SWAN in a shallow water application. Ocean Modelling 35, 215–229. URL: http://dx.doi.org/10.1016/j.ocemod.2010.07.009, doi:10.1016/j.ocemod.2010.07.009.

Clare, M.C., Kramer, S.C., Cotter, C.J., Piggott, M.D., 2022. Calibration, inversion and sensitivity analysis for hydro-morphodynamic models through the application of adjoint methods. Computers & Geosciences 163, 105104.

Dietrich, J.C., Zijlema, M., Westerink, J.J., Holthuijsen, L.H., Dawson, C., Luettich, R.A., Jensen, R.E., Smith, J.M., Stelling, G.S., Stone, G.W., 2011. Modeling hurricane waves and storm surge using integrally-coupled, scalable computations. Coastal Engineering 58, 45–65. URL: http://dx.doi.org/10.1016/j.coastaleng.2010.08.001, doi:10.1016/j.coastaleng.2010.08.001.

Dingemans, M., 1987. Verification of numerical wave propagation models with laboratory measurements: HISWA verification in the directional wave basin. h0228 .

Dobbelaere, T., Curcic, M., Le Hénaff, M., Hanert, E., 2022. Impacts of Hurricane Irma (2017) on wave-induced ocean transport processes. Ocean Modelling 171, 101947. URL: https://doi.org/10.1016/j.ocemod.2022.101947, doi:10.1016/j.ocemod.2022.101947.

Donelan, M.A., Hamilton, J., Hui, W., 1985. Directional spectra of wind-generated ocean waves. Philosophical Transactions of the Royal Society of London. Series A, Mathematical and Physical Sciences 315, 509–562.

Duncan, J., 1981. An experimental investigation of breaking waves produced by a towed hydrofoil. Proceedings of the Royal Society of London. A. Mathematical and Physical Sciences 377, 331–348.

Dutour Sikirić, M., Roland, A., Janeković, I., Tomazić, I., Kuzmić, M., 2013. Coupling of the Regional Ocean Modeling System (ROMS) and Wind Wave Model. Ocean Modelling 72, 59–73. doi:10.1016/j.ocemod.2013.08.002.

Eldeberky, Y., Battjes, J.A., 1996. Spectral modeling of wave breaking: Application to Boussinesq equations. Journal of Geophysical Research: Oceans 101, 1253–1264.

Funke, S.W., Farrell, P.E., Piggott, M., 2014. Tidal turbine array optimisation using the adjoint approach. Renewable Energy 63, 658–673.

Hasselmann, K., Barnett, T.P., Bouws, E., Carlson, H., Cartwright, D.E., Eake, K., Euring, J.A., Gicnapp, A., Hasselmann, D.E., Kruseman, P., Meerburg, A., Mullen, P., Olbers, D.J., Richren, K., Sell, W., Walden, H., 1973. Measurements of wind-wave growth and swell decay during the joint North Sea wave project (JONSWAP). .

Holthuijsen, L.H., 2010. Waves in oceanic and coastal waters. Cambridge university press.

Hutton, E., Piper, M., Tucker, G., 2020. The Basic Model Interface 2.0: A standard interface for coupling numerical models in the geosciences. Journal of Open Source Software 5, 2317. doi:10.21105/joss.02317.

Johnson, K., Kerr, S., Side, J., 2012. Accommodating wave and tidal energy - Control and decision in Scotland. Ocean and Coastal Management 65, 26–33. URL: http://dx.doi.org/10.1016/j.ocecoaman.2012.04.018, doi:10.1016/j.ocecoaman.2012.04.018.

Jonsson, I.G., Skougaard, C., Wang, J.D., 1970. Interaction between waves and currents, in: Coastal Engineering 1970, pp. 489–507.

Jordan, C., Dundovic, D., Fragkou, A.K., Deskos, G., Coles, D.S., Piggott, M.D., Angeloudis, A., 2022. Combining shallow-water and analytical wake models for tidal array micro-siting. Journal of Ocean Engineering and Marine Energy 8, 193–215. URL: https://doi.org/10.1007/s40722-022-00225-2, doi:10.1007/s40722-022-00225-2.

Kärnä, T., 2020. Discontinuous Galerkin discretization for two-equation turbulence closure model. Ocean Modelling , 101619URL: https://doi.org/10.1016/j.ocemod.2020.101619, doi:10.1016/j.ocemod.2020.101619.

Kärnä, T., de Brye, B., Gourgue, O., Lambrechts, J., Comblen, R., Legat, V., Deleersnijder, E., 2011. A fully implicit wetting-drying method for DG-FEM shallow water models, with an application to the Scheldt Estuary. Computer Methods in Applied Mechanics and Engineering 200, 509–524. doi:10.1016/j.cma.2010.07.001.

Kärnä, T., Kramer, S.C., Mitchell, L., Ham, D.A., Piggott, M.D., Baptista, A.M., 2018. Thetis coastal ocean model: discontinuous galerkin discretization for the three-dimensional hydrostatic equations. Geoscientific Model Development 11, 4359–4382. URL: https://gmd.copernicus.org/articles/11/4359/2018/, doi:10.5194/gmd-11-4359-2018.

Komen, G.J., Cavaleri, L., Donelan, M., Hasselmann, K., Hasselmann, S., Janssen, P.A., 1996. Dynamics and modelling of ocean waves.

Kumar, N., Voulgaris, G., Warner, J.C., 2011. Implementation and modification of a three-dimensional radiation stress formulation for surf zone and rip-current applications. Coastal Engineering 58, 1097–1117. URL: http://dx.doi.org/10.1016/j.coastaleng.2011.06.009, doi:10.1016/j.coastaleng.2011.06.009.

Lai, R.J., Long, S.R., Huang, N.E., 1989. Laboratory studies of wave-current interaction: Kinematics of the strong interaction. Journal of Geophysical Research 94, 16201. doi:10.1029/jc094ic11p16201.

Longuet-Higgins, M., Stewart, R., 1964. Radiation stresses in water waves; a physical discussion, with applications doi:10.1109/TIE.2012.2208438.

Longuet-Higgins, M.S., Stewart, R.W., 1962. Radiation stress and mass transport in gravity waves, with application to 'surf beats'. Journal of Fluid Mechanics 13, 481–504. doi:10.1017/S0022112062000877.

Madsen, O.S., Poon, Y.K., Graber, H.C., 1989. Spectral wave attenuation by bottom friction: Theory, in: Coastal engineering 1988, pp. 492–504.

Marsooli, R., Orton, P.M., Mellor, G., Georgas, N., Blumberg, A.F., 2017. A coupled circulation-wave model for numerical simulation of storm tides and waves. Journal of Atmospheric and Oceanic Technology 34, 1449–1467. doi:10.1175/JTECH-D-17-0005.1.

Martins, K., Blenkinsopp, C.E., Deigaard, R., Power, H.E., 2018. Energy dissipation in the inner surf zone: New insights from LiDAR-based roller geometry measurements. Journal of Geophysical Research: Oceans 123, 3386–3407. doi:10.1029/2017JC013369.

Mellor, G., 2015. A combined derivation of the integrated and vertically resolved, coupled wave-current equations. Journal of Physical Oceanography 45, 1453–1463. doi:10.1175/JPO-D-14-0112.1.

Mellor, G.L., 1998. Users guide for a three dimensional, primitive equation, numerical ocean model. Citeseer. URL: http://www7.civil.kyushu-u.ac.jp/kankyo/adcp/2011/pom2k.pdf.

Mellor, G.L., Donelan, M.A., Oey, L.Y., 2008. A surface wave model for coupling with numerical ocean circulation models. Journal of Atmospheric and Oceanic Technology 25, 1785–1807. doi:10.5194/gmd-15-745-2022.

Pennock, S., Coles, D., Angeloudis, A., Bhattacharya, S., Jeffrey, H., 2022. Temporal complementarity of marine renewables with wind and solar generation: implications for gb system benefits. Applied Energy 319, 119276.

Peregrine, D.H., 1976. Interaction of waves and currents. Advances in applied mechanics 16, 9–117.

Rathgeber, F., Ham, D.A., Mitchell, L., Lange, M., Luporini, F., McRae, A.T., Bercea, G.T., Markall, G.R., Kelly, P.H., 2016. Firedrake: Automating the finite element method by composing abstractions. ACM Transactions on Mathematical Software 43. doi:10.1145/2998441, arXiv:1501.01809.

Reniers, A.J., Battjes, J.A., 1997. A laboratory study of longshore currents over barred and non-barred beaches. Coastal Engineering 30, 1–21. doi:10.1016/s0378-3839(96)00033-6.

Ris, R.C., Holthuijsen, L.H., 1996. Spectral modelling of current induced wave-blocking. Coastal Engineering Proceedings 25.

Roelvink, J., Reniers, A., 1995. LIP 11D delta flume experiments. Delft Hydraulics .

Roland, A., 2008. Development of WWM II: Spectral wave modelling on unstructured meshes. Doctoral dissertation, Ph. D. thesis, Technische Universität Darmstadt, Institute of Hydraulic and Water Resources Engineering .

Roland, A., Zhang, Y.J., Wang, H.V., Meng, Y., Teng, Y.C., Maderich, V., Brovchenko, I., Dutour-Sikiric, M., Zanke, U., 2012. A fully coupled 3D wave-current interaction model on unstructured grids. Journal of Geophysical Research: Oceans 117, 1–18. doi:10.1029/2012JC007952.

Santos, J.A., Guilherme, L., Fortes, C.J., Pinheiro, L., Simões, A., 2009. Coupling numerical models for wave propagation in the MOIA package. Journal of Coastal Research I, 544–548.

Svendsen, I.A., 1984. Wave heights and set-up in a surf zone. Coastal engineering 8, 303–329.

SWAN Team, 2019. Scientific and tehcnical documentation, SWAN Cycle III version 41.31A. Delft University of Technology arXiv:arXiv:1011.1669v3.

Tucker, G.E., Hutton, E.W.H., Piper, M.D., Campforts, B., Gan, T., Barnhart, R., Kettner, A., Overeem, I., Peckham, S.D., Mccready, L., Syvitski, J., 2021. CSDMS : A community platform for numerical modeling of Earth-surface processes , 1–40.

Venugopal, V., Wolfram, J., Linfoot, B.T., 2005. RR401 The properties of extreme waves , 90.

Warder, S.C., Angeloudis, A., Piggott, M.D., 2022. Sedimentological data-driven bottom friction parameter estimation in modelling bristol channel tidal dynamics. Ocean Dynamics 72, 361–382.

Warner, J.C., Sherwood, C.R., Signell, R.P., Harris, C.K., Arango, H.G., 2008. Development of a three-dimensional, regional, coupled wave, current, and sediment-transport model. Computers and Geosciences 34, 1284–1306. doi:10.1016/j.cageo.2008.02.012.

Willmott, C.J., 1981. On the validation of models. Physical geography 2, 184–194.

Wolf, J., Prandle, D., 1999. Some observations of wave–current interaction. Coastal Engineering 37, 471–485.

Xia, H., Xia, Z., Zhu, L., 2004. Vertical variation in radiation stress and wave-induced current. Coastal Engineering 51, 309–321. doi:10.1016/j.coastaleng.2004.03.003.

Xie, L., Wu, K., Pietrafesa, L., Zhang, C., 2001. A numerical study of wave-current interaction through surface and bottom stresses: Wind-driven circulation in the South Atlantic Bight under uniform winds. Journal of Geophysical Research: Oceans 106, 16841–16855.

Zhang, X., Simons, R., Zheng, J., Zhang, C., 2021. A review of the state of research on wave-current interaction in nearshore areas. Ocean Engineering 243, 110202. URL: https://doi.org/10.1016/j.oceaneng.2021.110202, doi:10.1016/j.oceaneng.2021.110202.

Zhang, Y., Baptista, A.M., 2008. SELFE: A semi-implicit Eulerian-Lagrangian finite-element model for cross-scale ocean circulation. Ocean Modelling 21, 71–96. doi:10.1016/j.ocemod.2007.11.005.

Zhang, Y.J., Ye, F., Stanev, E.V., Grashorn, S., 2016. Seamless cross-scale modeling with SCHISM. Ocean Modelling 102, 64–81. doi:10.1016/j.ocemod.2016.05.002.